TECHNIQUES FOR MASS DETERMINATION OF AIRBORNE MICRO-PARTICLES IN AN OPTICAL DIPOLE FORCE TRAP

GEHRIG MICHAEL ISAAC CARLSE

A THESIS SUBMITTED TO
THE FACULTY OF GRADUATE STUDIES
IN PARTIAL FULFILMENT OF THE REQUIREMENTS
FOR THE DEGREE OF

MASTER OF SCIENCE

GRADUATE PROGRAM IN PHYSICS AND ASTRONOMY
YORK UNIVERSITY
TORONTO, ONTARIO
AUGUST 2020

Abstract

We present the development of a new technique for rapidly measuring the masses of airborne particles confined in free space optical dipole force traps. This technique employs an ultrafast CMOS sensor with a wide field of view to image the real time motion of trapped particles on timescales in which diffusive Brownian motion predicted by Einstein makes a transition to ballistic motion. The technique relies on direct imaging of drop-and-restore experiments without the need for a vacuum environment. In these drop-and-restore experiments, the trapping light is rapidly shuttered with an acousto-optic modulator causing the particle to be released from and subsequently recaptured by the trapping force. The trajectories from the falls and restorations are combined to infer the particle mass, which we also corroborate using an analysis of position autocorrelation functions of the trapped particles. Using the drop-and-restore technique, we report a statistical uncertainty of less than 2% for masses on the order of 5×10^{-14} kg, using a data acquisition time of approximately 90 seconds. We also show that the measurement of a ballistic mean-squared displacement can be used for a preliminary estimate of the mass of a trapped micro-particle. Furthermore, we show that even the capacity to detect the timescale at which the transition to ballistic motion occurs, in combination with a measurement of particle size, can provide a similar mass estimate, consistent with the more rigorous mass determinations developed in this thesis. Ultimately, the methods presented here constitute simple, effective, and competitive alternatives for characterizing trapped particles and measuring their masses, in comparison with more elaborate standard techniques.

Acknowledgements

I cannot possibly fit a full description of everyone's contributions to this work without making these acknowledgements longer than my thesis itself. The tweezers project has been ongoing in our lab since... well, since before I was even a part of the 'our'.

I will do my best to acknowledge all of the contributions to this work, but also try to keep it brief, as there is so much to go around.

I would like to start by thanking Hermina Beica for the work that she did building up the optical tweezers experiment. Hermina, it is because of you that we are all in this mess. I am kidding, of course. I am constantly amazed at the amount of work that you put into this project to get it off the ground and keep it floating over the years. I will always be very grateful for the time that you took to explain and discuss the tweezers with me, but even more so I am thankful for your company and conversation that we shared which spanned certainly well beyond optics.

I would also like to thank Shira Jackson for her dedicated work in starting our

lab down this avenue of free-space trapping and helping to develop the ablation method which has served us so well.

Additionally, I would like to thank Andrew Vorozccovs, not only for helping to build the first optical tweezers experiments in our lab, but also for generously donating his time to discuss various imaging techniques and approaches with me well into the evening.

I definitely have to thank Jorge Perez-Garcia, The Captain, who was the first to work on the tweezers project with me. Jorge gave so many things to this work, from his dedication and creativity in pursuing different trappable particles, to his ever-expanding chemistry set which we used until the very end. It was a pleasure to sail the high seas with you.

I would also like to thank Boris Barron for his contributions to our theoretical understanding of the problems that we were facing, but also for gifting us with an invaluable and incredibly durable blue helmet, as well as a wonderfully distracting game of cards. Of course, Boris, Jorge, and myself, also share responsibility for some of the less fruitful attempts to atomize particles into the trap. Here, I think we would all agree that we learned a lot of practical lessons even if actual positive results were fewer and farther between.

I would really like to thank Alex Pouliot for the endless hours that he gave to me, going over theories, proposing different takes on the experiment (looking at you

Doppler-Tweezers), and always being up for a little tweezers-talk. I am particularly grateful for the, eventually almost daily, sanity checks when looking at a new set of data. More than this, I also greatly appreciate your efforts to get me to take a break and (you know... from time to time) get out of the lab to do something fun.

I would also like to thank Thomas Vacheresse for his never-ceasing positive attitude and enthusiasm which definitely kept me going particularly toward the end of that camera-Canada Day week, but also many a time since, when he sensed that he could help. I must also thank Tom for un-officially sponsoring all the computing necessary for these experiments. The contributions of t1, t2, t3, and t4 cannot be overlooked.

I have to thank Kevin Borsos for his incredible perseverance and for being the foil to my positive spin. I could not have asked for a better first mate or partner in crime. From taking and tracking many of our measurements, to the seemingly endless reading that you did on all things tweezers, thank you for sticking with the project even when all signs pointed to the need to abandon it.

I also thank Chris Wernik of Delta Photonics, who so generously arranged a week-long loan of the Phantom camera for us. Safe to say that without this enormous gift we would not have been able to pursue the avenues that we did.

I would like to thank Ozzy Mermut for her input and contributions to our project. She brought a sharp and refreshing perspective to our experiments at a time when we very much needed it.

I would also like to thank Matthew George, not only for his input and expertise but for the extra effort he made on our behalf, helping us track down and ultimately allowing us to borrow equipment, often without very much notice or a date of expected return. Matt, your flexibility and accommodation was appreciated more than I think you know.

I would also like to thank Louis Marmet for his insightful contributions both theoretically and experimentally. I am very grateful for the enthusiasm with which you dove into our otherwise mundane problems. Your perspectives were so very needed from your position slightly outside of our tweezers bubble. I would also like to thank you again for agreeing to serve on my committee where your input was all the more valuable.

In this same way, I would also like to thank Simone Pisana for serving as the Chair of my examining committee and bringing his own views to my work.

I would like to thank Marlene Caplan for helping me initially get into the MS program here at York, as well as Cristalina Del Biondo for helping me stay on track with the entire administrative side of my degree.

I would like to thank Chris Bergevin, for his consistent support and also his thoughtful inclusion of me in many opportunities that came his way. Additionally, I am grateful for his inquisitive presence, which made me think more deeply about many things, but also ultimately made me more deliberate in all of my pursuits.

I would like to thank Tom Kirchner for his help as the Graduate Programme Director. I think I spent more time in his office than I should have, but he was always very accommodating and incredibly patient with every problem that I brought upstairs.

Of course, I have to thank my supervisor Dr. A. Kumarakrishnan. I am incredibly grateful for all of the opportunities (which were inumerable) and support (which was immeasurable) that Kumar has given me, but also for the open and frank communication that he and I have always been able to have.

More directly however, Kumar, thank you for allowing us to take such ownership over the tweezers project. You gave us such a unique experience in this regard. You really empowered the entire tweezers team so that we felt as if we could direct not only the measurements but the trajectory of the experiment as a whole. All the while, Kumar, it was really your drive for the project that essentially brought the tweezers project back from the grave and kept it alive.

Lastly, to my family, I would like to thank you for supporting me in all the ways that you do, both big and small.

Table of Contents

List of Tables

List of Figures

Abbreviations

Abbreviation	**Long-form name**
AOM	Acousto-optic modulator
CoM	Center-of-mass
DoF	Depth of field
FORT	Far off-resonant trap
MSD	Mean-squared displacement
NA	Numerical aperture
ODF	Optical-dipole force
PACF	Position autocorrelation function
PSD	Power spectral density
QPD	Quadrant photodiode
ROI	Region of interest
TA	Tapered amplifier
VACF	Velocity autocorrelation function

1 Introduction

The main goal of this thesis is to discuss the development of a new technique for measuring the mass of airborne particles confined in free space optical dipole force (ODF) traps, also known as optical tweezers. The technique involves observing the trajectories of a trapped particle as it is released (dropped) from and recaptured (restored) to the equilibrium position of the trap to infer the mass of the particle [1]. At the heart of this technique is an ultrafast CMOS sensor with a wide field of view that is used to image the real time motion of trapped and freely-falling particles on fast timescales. In pursuit of mass determinations, we leverage the fast time resolution to investigate the transition regime where diffusive Brownian motion gives way to ballistic inertial motion. This work presents simple and competitive alternatives to more elaborate, conventional techniques for both characterizing trapped particles and measuring their masses.

1.1 Optical Tweezers, Video Microscopy, and Precise Mass Measurements

The development of ODF laser traps to confine dielectric particles [2–6] has had an incredibly wide-spread effect on scientific research. The myriad applications for ODF traps range from the development of far-off resonance traps (FORTs) for confining atoms [7, 8], to the manipulation of biological molecules with optical tweezers [9]. ODF traps have been used in experiments to generate three-dimensional optical crystals [10, 11], as well as to make measurements of bond strengths [12] and protein synthesis inside living cells [13, 14]. However, despite all of these other pursuits, one of the most fruitful avenues of research that optical tweezers has advanced is the investigation of single particle motion.

With ever-improving bandwidth [15] and spatial resolution [16] in positional detectors, optical tweezers experiments have been able to push the boundaries of investigation to shorter time and length scales. The natural progression of this field has led to powerful experiments investigating the diffusive kinematics of single particles trapped in fluids and free space. The pioneering experiments in references [17–21] have probed the timescales on which diffusive Brownian motion transitions to ballistic motion. Other lines of inquiry have focused on particle kinematics to study the nature of the ODF itself [22–24], the colour of the stochastic force associated with Brownian motion [25], the development of precise force sensors [26], as well as measurements of fluid viscosity [27, 28] and the polarizability [29] of trapped particles. These experiments have employed complementary techniques, such as analyses of power spectra [30, 31] and autocorrelation functions of the particle motion [17, 19].

Recently, there has also been widespread interest in employing optical tweezers to perform precise mass measurements of trapped particles [1, 32–36]. Table 1.1 shows a representative compilation of such tweezers related techniques. The most sensitive and accurate mass measurement involving optical tweezers has been obtained using underdamped ODF traps operated in a vacuum environment [35]. In reference [35], the trapped particle is driven using an alternating electric field and the mass is determined by fitting to the power spectral density (PSD). This technique has been successful in characterizing masses of $\sim 4 \times 10^{-18}$ kg, with a precision of 0.25%. Other examples of tweezers-based mass determinations in the range of $10^{-10} - 10^{-15}$ kg involve photophoretic traps [33] and have achieved precision at the level of a few percent [32, 37].

In the body of this thesis, I will discuss a simple free space optical tweezers set-up in which scattered light from trapped particles can be directly imaged using high-speed video microscopy. I will investigate the prospects of using such an apparatus as a tool to study Brownian motion at the onset of the ballistic regime of micro-

Table 1.1: Summary of contemporary tweezers-based mass measurements. The last column shows the statistical (Stat.) and systematic (Syst.) uncertainties associated with each measurement technique. * Indicates a measurement performed in a vacuum environment. ** Indicates a solution based measurement. *** Indicates a photophoretic trapping experiment in free space. VACF stands for velocity autocorrelation function.

Reference	Year	Technique	Mass (kg)	Stat. & Syst. Uncertainty
Huang et al. [17]**	2011	Continuous VACF analysis	1.26×10^{-14}	<10% and <10%
Lin et al. [32]***	2017	Optically forced modulation	9.00×10^{-13}	2% and 6%
Chen et al. [33]***	2018	Dynamic power-modulation	6.3×10^{-15}	Not estimated
Blakemore et al. [34]	2019	Electrostatic co-levitation	8.40×10^{-15}	1% and 1.8%
Ricci et al. [35]*	2019	Electrostatically driven resonance	4.01×10^{-18}	0.25% and 0.5%
This work [1]	2020	Drop-and-restore	5.58×10^{-14}	1.4% and 13%

particle motion, as opposed to other indirect measurement techniques. I will also show how measurements of such ballistic motion can be used, independently and in combination with particle size determinations, to infer preliminary estimates of the mass of trapped particles. Building on this work, I will demonstrate that the use of such an apparatus to track the release and recapture of particles held in a single-beam gradient trap can result in a simple technique for the rapid and precise determination of the particle masses. Using methods that are similar to techniques for studying the ballistic expansion of ultracold atomic samples [38], we track the centroid of particles dropped in free space to infer the damping rate and analyze the trajectory of the recaptured particle to determine the particle mass. This methodology relies on the precise timing for the release and recapture of trapped particles, enabled by laser amplitude modulation using an acousto-optic modulator (AOM). As a result, we can combine the advantages of tight confinement in an ODF trap and the capacity to observe the free space kinematics sensitively as in the drop tower studies of [39]. In contrast with our investigations of ballistic Brownian motion using the same apparatus, we average uncorrelated repetitions of these drop-and-restore measurements so that the effect of Brownian noise on short timescales is suppressed, thereby, increasing the signal-to-noise ratio even at very short camera exposure times. This leads to a measurement with a unique combination of short time resolution and high signal-to-noise ratio from which a highly precise mass determination can be extracted. To further support these findings, I also present a corroboration of these measurements through separate studies of the position autocorrelation function (PACF), that are more in line with conventional single particle techniques. I will show that masses on the order of 10^{-14} kg associated with resinous particles with diameters of a few micrometers can be determined with a statistical precision of $\sim 2\%$ in measurement times on the order of 1 minute, results that suggest the technique is suitably competitive.

In Chapter 2, I describe the theoretical framework for particle kinematics and the features of the PACFs which feature in this work. Chapter 3 describes the experimental set-up, and the main results of these investigations are presented in Chapter 4, while Chapter 5 summarizes the work and outlines some future directions of inquiry.

2 Theory

This chapter consists of three sections in which I outline the basis for the rest of this thesis. First, in Section 2.1, I present some of the theory governing optical tweezers, including a derivation of the relevant forces in the Rayleigh scattering limit, as well as a discussion of extensions to both the geometric optics and Mie scattering regimes. Next, in Section 2.2, I discuss Brownian motion in more detail, both in general and in relation to optically trapped particles. I review the theory which underpins Brownian motion and estimate the timescales for ballistic and diffusive motion. Finally, in Section 2.3, I present the kinematics most relevant to the drop-and-restore mass determination technique, which rests on the intersection of optical tweezers and Brownian motion.

2.1 Basic Theory of Optical Tweezers

The derivation of the forces involved in optical tweezers has been a point of contention since the inception of the technique.

There are two distinct schools of thought on how to describe these forces and each depends on the answer to a key question: “What is the size of the particle a, in relation to the wavelength of the light, λ?”

The first of these arguments addresses the so-called “geometric limit”, where the size of the particle greatly exceeds the wavelength of light ($a \gg \lambda$). Arthur Ashkin developed a highly accurate description for his experiments on the basis of ray optics, where individual rays of light are refracted by the particle [40]. In this formulation, the ensuing momentum changes of these rays due to the relative indices of refraction of the surrounding medium (air) and the particle are calculated. Then, by assuming an opposing force imparted on the particle, the net optical dipole force on the particle can also be computed. A brief schematic of this approach for a dielectric sphere in a vertically focussed Gaussian beam is shown in Figure 2.1. Variations of this sort of framework have been shown to work quite well even as the particle size becomes as small as 5λ, but these treatments break down near the beam focus [41].

The second, and perhaps simpler approach to understanding the ODF, involves the “Rayleigh approximation”, which considers particles that are much smaller than the wavelength of light ($a \ll \lambda$) and deals with the induced dipole moment of the particle. A complete treatment in this limit is presented in reference [42], where for a dielectric particle of radius r_s and dielectric constant ϵ_1, we can describe the

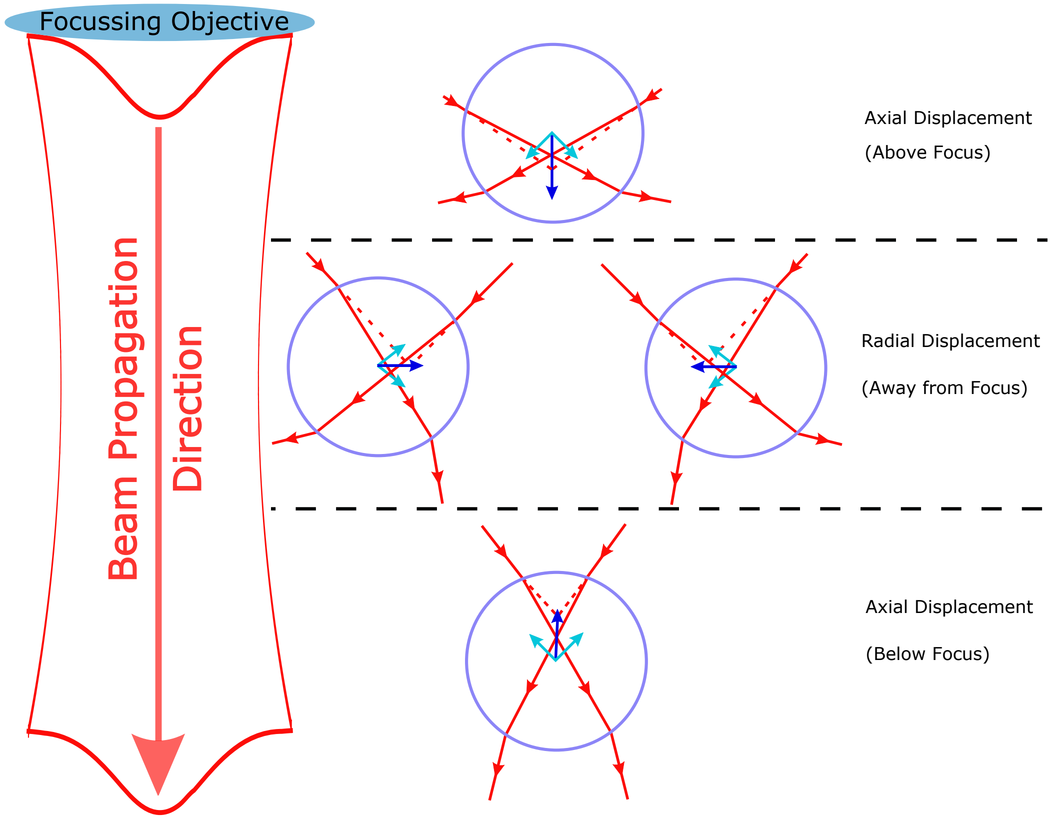

Figure 2.1: Schematic diagram of an ODF trap in the geometric regime. Here, the pale blue circle indicates a trapped dielectric sphere and the red lines indicate the paths of two rays of focussed laser light. The dashed lines indicate the original (unrefracted) path leading to the geometric focus of the beam. The cyan lines indicate the reaction forces on the sphere resulting from momentum transfer imparted by light and the dark blue lines indicate the net force on the sphere.

induced dipole moment as:

$$\begin{aligned}\vec{p}(\vec{x},t) &= 4\pi\epsilon_2 r_s^3 \frac{\epsilon_1-\epsilon_2}{\epsilon_1+2\epsilon_2}\vec{E}(\vec{x},t)\\ &= 4\pi n_2^2\epsilon_0 r_s^3 \frac{\mu_n^2-1}{\mu_n^2+2}\vec{E}(\vec{x},t)\end{aligned} \tag{2.1}$$

where $\vec{E}(\vec{x},t)$ represents the electric field of the laser as a function of generalized position co-ordinate $\vec{x}$ and time t, while ϵ_2 is the dielectric constant of the medium surrounding the particle, and $\mu_n = n_1/n_2$ is the ratio of the indices of refraction for the particle (n_1) and the surrounding medium (n_2).

The laser field exerts an intensity dependent force on this dipole, that is conventionally broken down into two components:

$$\vec{F}(\vec{x},t) = \vec{F}_{OD} + \vec{F}_{RP} \tag{2.2}$$

$\vec{F}_{OD}$ is known as the optical dipole or gradient force and $\vec{F}_{RP}$ is known as the scattering or radiation pressure force. Since the first term in equation 2.2 is of greater interest in the context of this thesis, I next present a brief derivation of the optical dipole force, and simply state the result for the scattering force as developed in reference [42].

2.1.1 Gradient Force

We begin with the force on the induced dipole, which is written as:

$$\vec{F}_{OD}(\vec{x},t) = \left(\vec{p}(\vec{x},t)\cdot\nabla\right)\vec{E}(\vec{x},t) \tag{2.3}$$

where, by taking the time average over many periods of the electric field, (denoted by $\langle ... \rangle_{\lambda/c}$) we find that the force scales as the gradient of the laser intensity, $\nabla I(\vec{x})$:

$$\begin{aligned} \langle \vec{F}_{OD}(\vec{x},t)\rangle_{\lambda/c} &= 4\pi n_2^2 \epsilon_0 r_s^3 \frac{\mu_n^2-1}{\mu_n^2+2}\frac{1}{2}\nabla\langle \vec{E}(\vec{x},t)^2\rangle_{\lambda/c} \\ &= \pi n_2^2 \epsilon_0 r_s^3 \frac{\mu_n^2-1}{\mu_n^2+2}\nabla |E(\vec{x})|^2 \\ &= \alpha \nabla I(\vec{x}) \end{aligned} \tag{2.4}$$

with a coupling constant $\alpha = \frac{2\pi n_2 \epsilon_0 r_s^3}{c}\frac{\mu_n^2-1}{\mu_n^2+2}$, proportional to the polarizability of the sphere.

We note one important feature common to all these theoretical methods which is particularly evident in equation 2.4, namely that the dipole force acts as a restoring force towards the location of maximum laser intensity. This holds true in situations where the index of refraction of a particle is higher than that of the surrounding media, which is to say $\mu_n > 1$. For cases where the index of the particle is lower than that of the medium, the force changes sign and is no longer restorative. In both cases, the force remains proportional to the gradient in the light intensity. As such, we turn our attention in the next section to a description of the laser field.

2.1.1.1 Discussion of Intensity Gradients

For a Gaussian laser beam (TEM_{00}) propagating along the $\widehat{z}$ direction, we can model the intensity profile as:

$$I(r,z) = I_0(z)e^{\frac{-2r^2}{\omega'(z)^2}} \tag{2.5}$$

where $I_0(z)$ represents the peak intensity of the beam, $\omega'(z)$ represents the beam waist, and r represents the radial co-ordinate.

Assuming that the total power P in an axial direction is conserved, we can write:

$$P = \iint I(r,z)drd\theta = \frac{\pi\omega'(z)^2}{2}I_0(z) \tag{2.6}$$

where as the beam propagates, the radius of the beam obeys:

$$\omega'(z) = \omega_m\sqrt{1+(\frac{z}{z_0})^2} \tag{2.7}$$

with z_0 representing the Rayleigh range and ω_m indicating the minimum $1/e^2$ beam radius.

Accordingly, equation 2.5 can be re-written as:

$$\begin{aligned} I(r,z) &= \frac{2P}{\pi\omega'(z)^2}e^{\frac{-2r^2}{\omega'(z)^2}} \\ &= \frac{2P}{\pi\omega_m^2(1+(\frac{z}{z_0})^2)}e^{\frac{-2r^2}{\omega'(z)^2}} \end{aligned} \tag{2.8}$$

In this manner, the intensity gradients along both the axial and radial directions can be determined by differentiating equation 2.8, yielding:

$$\frac{\partial}{\partial r}I(r,z) = \frac{-4r}{\omega'(z)^2}I(r,z) \tag{2.9a}$$

$$\frac{\partial}{\partial z}I(r,z) = \frac{-2z\omega_m^2}{z_0^2\omega'(z)^2}\left(1-\frac{2r^2}{\omega'(z)^2}\right)I(r,z) \tag{2.9b}$$

Here, we can see the negative signs in both equations demonstrating the position-dependent nature of the ODF described by equation 2.4.

2.1.2 Scattering force

In contrast to the gradient force, the radiation pressure force always points in the same direction, namely along the direction of beam propagation, $\widehat{z}$. This can be shown by writing the force in terms of a scattering cross-section σ_p and the Poynting vector $\vec{S}(\vec{x},t)$:

$$\vec{F}_{RP}(\vec{x},t) = \frac{\sigma_p\vec{S}(\vec{x},t)}{c/n_2} \tag{2.10}$$

By again taking the time average over many periods of the laser's electric field we can arrive at the expression:

$$\begin{aligned}\langle\vec{F}_{RP}(\vec{x},t)\rangle_{\lambda/c} &= \frac{\sigma_p n_2\langle\vec{S}(\vec{x},t)\rangle_{\lambda/c}}{c}\\ &= \frac{n_2\sigma_p}{c}I(\vec{x})\widehat{z}\end{aligned} \tag{2.11}$$

To compare this force with the optical dipole force given by equation 2.4, we can write out this cross section as in reference [42]:

$$\sigma_p = \frac{8}{3}\left(\frac{2\pi r_s}{\lambda}\right)^4 r_s^2 \left(\frac{\mu_n^2 - 1}{\mu_n^2 + 2}\right)^2 \tag{2.12}$$

Here, we see that only the square of the fraction $\frac{\mu_n^2-1}{\mu_n^2+2}$ appears, resulting in a unidirectional force, independent of the index of refraction of the particle.

2.1.3 General Remarks

Taking both of the force components into consideration, we can then rewrite equation 2.2 as:

$$\vec{F}(\vec{x},t) = \alpha\nabla\cdot I(\vec{x}) + \frac{n_2\sigma_p}{c} I(\vec{x})\widehat{z} \tag{2.13}$$

Unfortunately, while equation 2.13 is instructive as to the qualitative behaviour of an optical trap, it cannot be used to make meaningful magnitude estimates of the trapping forces discussed in this thesis, where the particle size is slightly larger than the wavelength of light ($a > \lambda$). Despite its compact notation, the Rayleigh approximation, like the geometric limit, does not extend easily over the range of particle sizes typically used in optical tweezers experiments ($a \sim \lambda$). This "in-between" size scale has been approached from either side with higher order corrections to both Mie-Lorentz and Rayleigh scattering formalisms [43–46]. However, due to the complexity of these treatments, the nature of the light matter interaction is more readily quantified empirically in practical optical tweezers experiments.

To second order, most, if not all, of these treatments yield harmonic oscillator-like potentials. Accordingly, when particles trapped in such potentials are buffeted from collisions with the surrounding medium, they undergo confined random walks. Thus to better approach this problem, we turn our attention to the behaviour of these harmonically confined microscopic particles, rather than further investigate the light-matter interaction. In what follows, we will develop a more complete understanding of the kinematics on the time and length scales of Brownian motion, and examine how this Brownian behaviour changes when constrained in a tweezers-like potential.

2.2 Brownian Motion

2.2.1 Unconstrained Brownian Motion

The behaviour of simple diffusive Brownian motion, was perhaps most concisely phrased by Langevin's equation of motion [47] which is given by:

$$m\frac{\partial^2 x}{\partial t^2} + \gamma\frac{\partial x}{\partial t} = F(t) \tag{2.14}$$

where m is the mass of the particle, γ is the Stokes damping coefficient, and $F(t)$ is the stochastic force responsible for Brownian motion.

Equation 2.14, captures the trajectories and mean-squared displacement (MSD) initially observed by Brown [48], while also including the inertia of Brownian particles, previously omitted from the statistical description predicted by Einstein [49].

From a general perspective, the MSD can be derived from the position-time series of a particle $x(t)$:

$$\begin{aligned}\langle[\Delta x(t)]^2\rangle &= \langle(x(t_0+t)-x(t_0))^2\rangle \\ &= \langle(x(t_0+t)^2 - 2(x(t_0+t)x(t_0)) + x(t_0)^2)\rangle\end{aligned} \tag{2.15}$$

where, t_0 is some initial time relative to t. If, however, the process governing the motion is truly stochastic, then there will be no difference between any two average positions $\langle x(t_0)\rangle$ and $\langle x(t)\rangle$, such that:

$$\begin{aligned}\langle[\Delta x(t)]^2\rangle &= \langle 2(x(t_0+t)^2 - x(t_0+t)x(t_0))\rangle \\ &= 2\langle x(t_0+t)^2\rangle - 2\langle x(t_0)x(t_0+t)\rangle\end{aligned} \tag{2.16}$$

where, the first term is just the variance of particle motion, and the second term in this equation is known as the position auto-correlation function (PACF), which is the Fourier transform of the power spectral density (PSD) [30].

For the case of unconstrained Brownian motion, the full MSD is given by:

$$\begin{aligned}\langle[\Delta x(t)]^2\rangle &= \langle(x(t_0+t)-x(t_0))^2\rangle \\ &= 2k_BT\gamma^{-1}t - \frac{2k_BTm}{\gamma^2}(1-e^{-\frac{\gamma t}{m}})\end{aligned} \tag{2.17}$$

for $t_0 = 0$, where k_B is the Boltzmann constant and T is the temperature [50].

For this type of unconstrained random walk, equations 2.17, and by extension

2.16, both have simple behaviours at long times:

$$\begin{aligned}\langle[\Delta x(t \gg 0)]^2\rangle &\sim 2k_B T\gamma^{-1}t \\ &\sim 2Dt\end{aligned} \tag{2.18}$$

where, $D = k_B T/\gamma$ is the diffusion constant. In effect, this is the statistical result predicted by Einstein [49]. An illustration of equations 2.17 and 2.18 is shown in Figure 2.2, highlighting the agreement of both descriptions for a random walker at $t \gg 0$.

However, if such a random walker is confined in a harmonic potential, as shown in Figure 2.3, the trajectory of the particle, particularly at long times, is drastically altered. Unsurprisingly, the confinement causes a similarly prominent change in the long-time behaviour of the MSD. To better understand this, in the next section, we focus on the case of constrained Brownian motion, and reserve discussion of the deviations from Einstein's predictions at short times to Section 2.2.3 where we will look more closely at this inertial motion.

2.2.2 Constrained Brownian Motion

With the advent of lasers and optical tweezers, the observation of confined single particles became not only possible, but also fairly easy to realize. As noted in the introductory section, this has lead to significant advancements in the field of Brownian kinetics based on the details of looking deeply at a stochastically driven

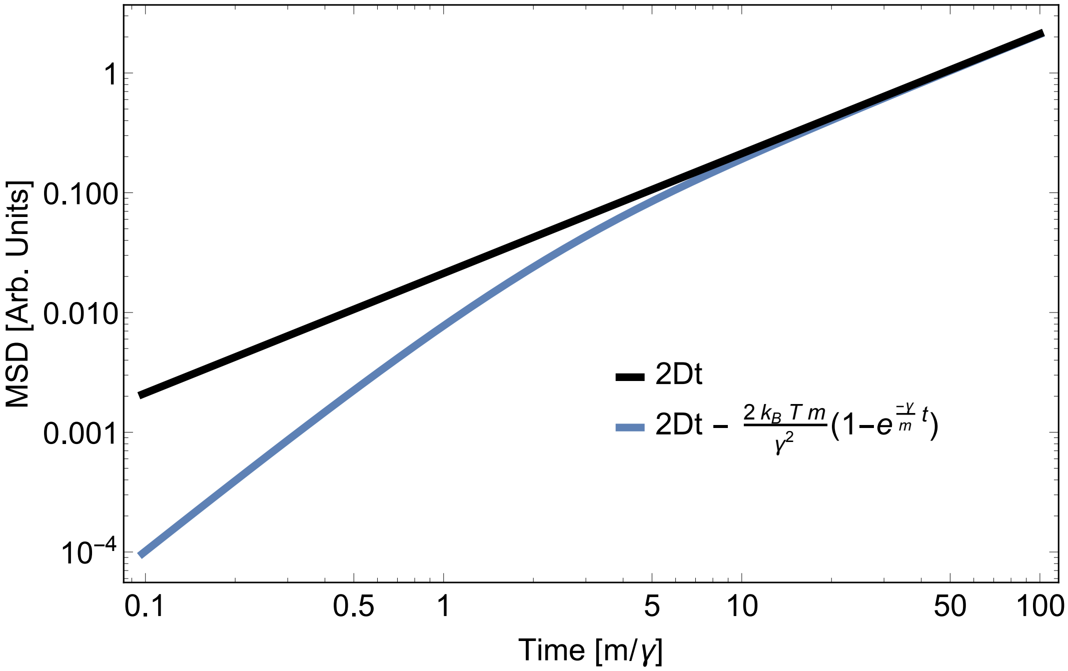

Figure 2.2: Illustration of the theoretical MSD for a Brownian particle. The black line shows the statistical prediction of Einstein (equation 2.18), while the blue curve models the case including particle inertia using equation 2.17. These curves assume $T = 300$ K, $m = 5 \times 10^{-14}$ kg, and $\gamma = 7.6 \times 10^{-10}$ kg/s.

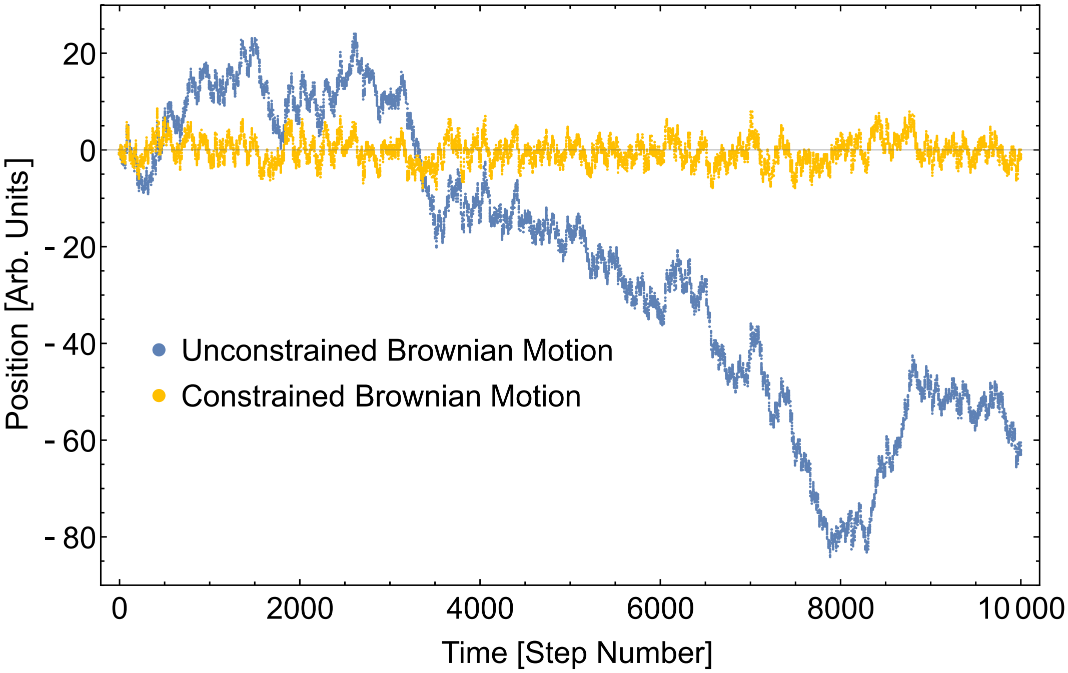

Figure 2.3: Simulated trajectory of free and harmonically constrained random walkers over a 10000-step trajectory.

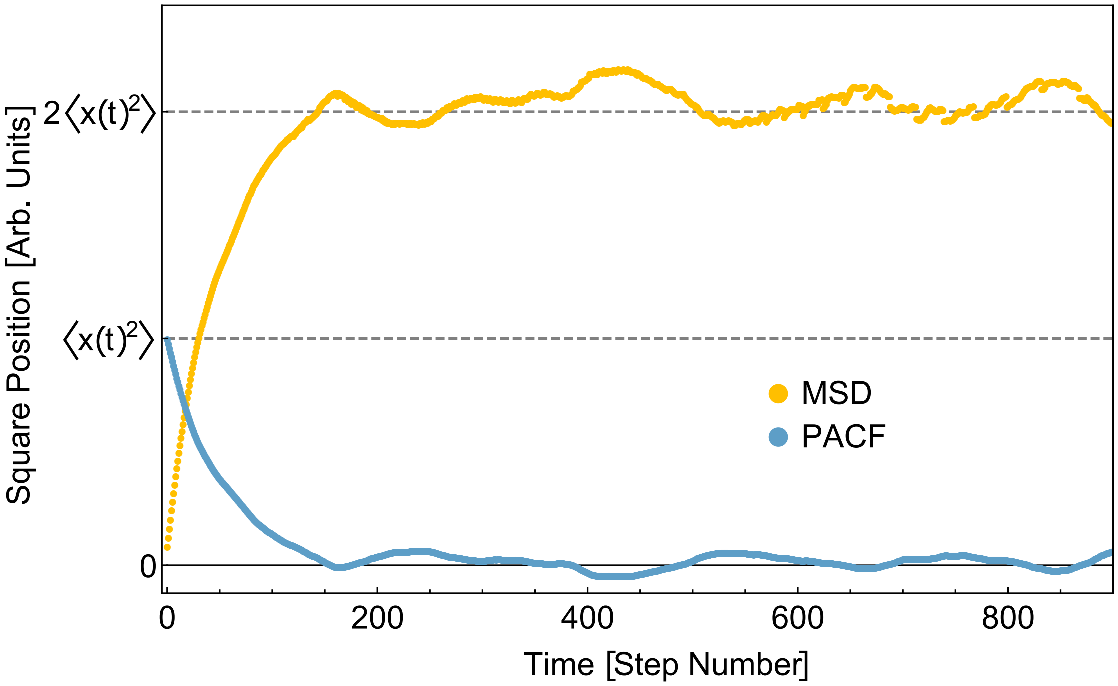

Figure 2.4: MSD and PACF of the simulated constrained random walker shown in Figure 2.3. The dashed lines show scalar multiples of the variance on the same unit scale. See Appendix A for a discussion of the MSD of discrete time series.

particle trapped in a harmonic potential, as described by:

$$\frac{\partial^2 x}{\partial t^2} + \Gamma \frac{\partial x}{\partial t} + \frac{\kappa}{m} x = A(t) \tag{2.19}$$

where $\Gamma = \frac{\gamma}{m}$ is the damping rate, κ is the spring constant of the ODF trap, and $A(t) = F(t)/m$ is the random acceleration associated with the stochastic force.

When considering the MSD for such a system, it is convenient to independently consider the two terms in equation 2.16. For a sufficiently long time series, the variance for a harmonically constrained random walk will flatten out to a stable level which characterizes the strength of the confinement. Typically, this steady-state variance is described by a version of the equipartition theorem given by [51]:

$$\frac{1}{2}\kappa\langle x(t)^2\rangle = \frac{1}{2}k_BT \tag{2.20}$$

where, the potential energy of the ODF trap is equated to the thermal energy of the particle defined by the Boltzmann constant and the temperature T. In contrast, the autocorrelation function approaches zero at long times, due to the continued random nature of the steps about the equilibrium position in the trap. These two constituent parts lead to an MSD of the form illustrated in Figure 2.4.

The specific behaviour of both the PACF and PSD, have been calculated [50, 52] for the overdamped, underdamped, and critically damped regimes of harmonic traps. The level of damping is typically characterized by the parameter $b = \frac{1}{2}\sqrt{\Gamma^2 - 4\omega_0^2}$, where $\omega_0 = \sqrt{\frac{\kappa}{m}}$ is the natural angular frequency of the trap [53].

Systems involving airborne micro-particles at atmospheric pressure are usually highly overdamped, meaning that b can be shown to have real roots [19, 51]. A simple estimate of the damping, for a particle of mass $m \sim 10^{-13}$ kg and radius $r_s \sim 3$ μm, can be found in Section 2.2.4. The resulting overdamped PACF, which is of interest in the free-space experiments discussed in this thesis, is given by:

$$\langle x(t_0)x(t_0+t)\rangle = \frac{k_BT}{m\omega_0}e^{\frac{-\gamma}{2m}t}(\cosh(bt)+\frac{\gamma}{2mb}\sinh(bt)) \tag{2.21}$$

To investigate ballistic Brownian motion, one can also easily derive the relationship between such PACFs and their accompanying velocity autocorrelation functions (VACFs) [53]. These types of calculations have been of great value in measurements of instantaneous velocities, particularly in under-damped cases where the effects of the trapping potential on the particle motion are less apparent [19]. The reconstruction of correlation functions with high time-resolution has proven to be a highly effective method for determining particle size and mass [17]. In the work presented in this thesis, we use a version of the overdamped PACF to corroborate the mass measurements obtained through our drop-and-restore experiments.

Given that our work describes a highly overdamped case ($\Gamma^2 \gg 4\omega_0^2$), it is possible to further approximate equation 2.19 by omitting the inertial term, as in reference [54], so that the equation of motion becomes:

$$\gamma\frac{\partial x}{\partial t} + \kappa x = F(t) \tag{2.22}$$

resulting in the simplified autocorrelation function:

$$\langle x(t_0)x(t_0+t)\rangle = \frac{k_BT}{m\omega_0}e^{-t/\tau_0} \tag{2.23}$$

with a well defined time constant, known as the correlation time $\tau_0 = \frac{\gamma}{\kappa}$.

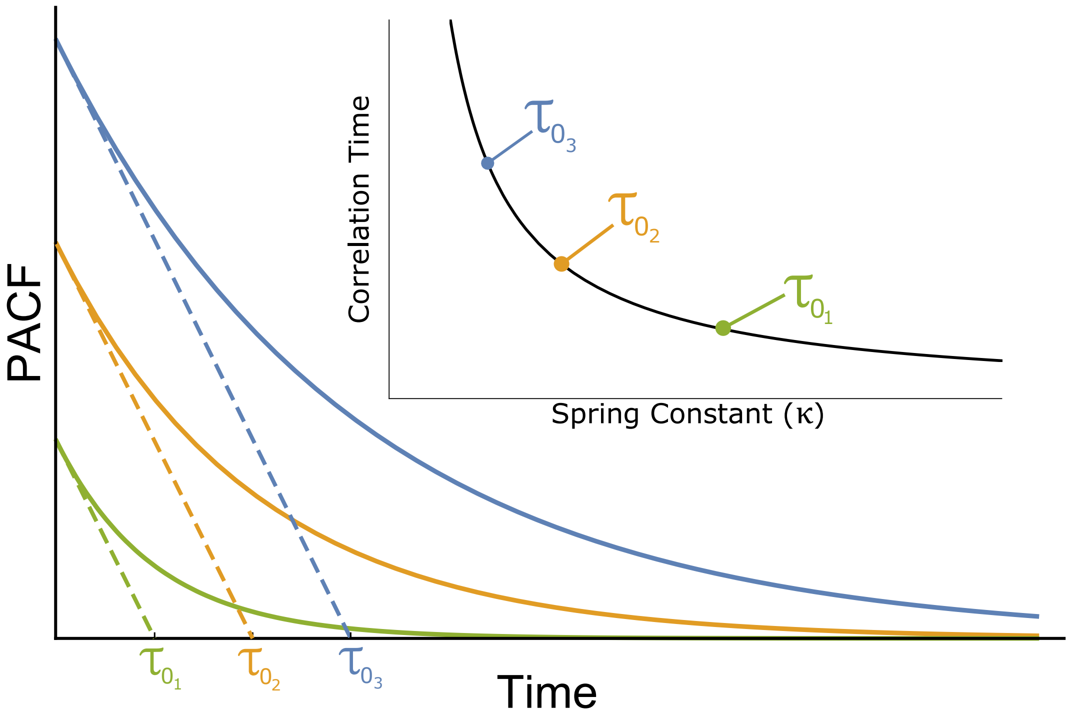

Figure 2.5: Illustration of the overdamped PACF described by equation 2.23. Each curve represents the PACF of a particle confined in an ODF trap with a different spring constant. The correlation time constants are shown at the base of the dashed lines. The expected $\frac{1}{\kappa}$ trend in the correlation time as a function of trap spring constant is shown as an inset.

An illustration of overdamped PACFs and the expected dependence of the correlation times on trap stiffness is shown in Figure 2.5. Due to the simple functional form of equation 2.23, τ_0 can easily be extracted from PACFs for ODF traps of different spring constants, leading to a precise determination of the damping coefficient γ from fits similar to the type shown in the inset of Figure 2.5.

Even though this degree of simplicity is not present for all levels of damping, the correlation time ratio γ/κ is relevant in all tweezers experiments as it determines the timescale on which the confining force interrupts the motion of the particle. Accordingly, we can see that before this interruption time, the behaviour of a constrained walker remains relatively unchanged compared to unconstrained Brownian motion [19]. It is for this reason that tweezers can serve as such an effective tool in the study of not only constrained but also free Brownian motion, if the required time resolution requirements can be met. This task has been greatly simplified by improvements in technology that have made it possible to track particles on increasingly short time and length scales.

2.2.3 Short-time Brownian Motion

Despite the elegance and simplicity of his 1905 paper [49], Einstein predicted that his scaling law, derived from a statistical treatment of gases, would ultimately break down at short times due to the inertial term included in the Langevin equation

(equation 2.14).

A complete treatment of such a random process including particle inertia was not long in development for both free and harmonically constrained stochastic particles [50, 52]. In both cases, the PACF (and thereby the MSD) were shown to deviate from Einstein's scaling law at short times.

An intuitive illustration of this phenomenon can be developed by first considering a particle moving in a vacuum. If moving at a constant speed, the particle displacement proceeds ballistically, which is to say, it scales as t, and the resulting MSD becomes quadratic. When this particle is instead placed in some media, collisions between the particle and the media restrict this ballistic motion. However, there still exists a period of time before the collisions can successfully damp the otherwise ballistic motion of the particle. It is this time scale which is often referred to as the momentum relaxation time τ_p.

A computational demonstration is shown in Figure 2.6, where the simulated constrained Brownian motion from Figure 2.3 is displayed with the random steps broken up into a more continuous path representing the trajectory at a finer time resolution. In Figure 2.6a, each macroscopic random step is partitioned into ten smaller time steps simulating a straight line trajectory that the particle would follow. The corresponding MSD for this motion is also shown in Figure 2.6b. We can clearly see a non-linear component of the MSD at times shorter than those of

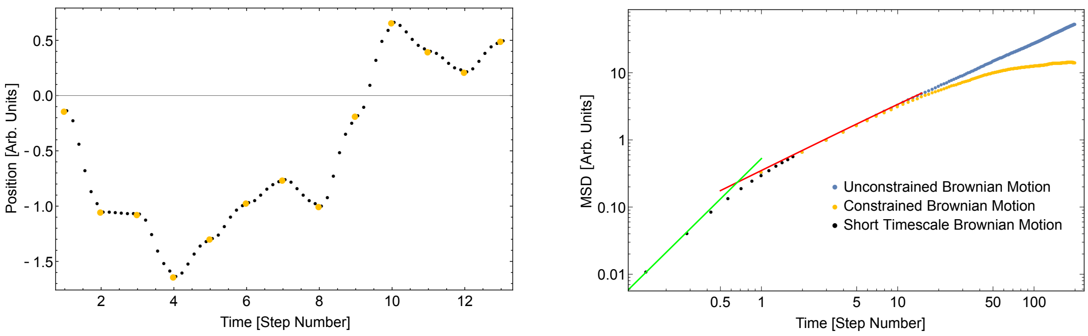

(a)

(b)

Figure 2.6: (a) Simulated trajectory excerpt for the harmonically constrained damped random walker shown in Figure 2.3. Random walk steps are shown as yellow points, linked with a curvilinear path (shown in black dots) representing the approximately linear ballistic short timescale motion of the same random walker. (b) The yellow points show the MSD computed from a random walk of the type shown in part (a). The blue data points show a simulation of the unconstrained random-walker shown in Figure 2.3. The black points show the MSD for the short-time resolution shown in black in part (a). The red line indicates a slope of 1 on the Log-Log graph consistent with diffusive Brownian motion (MSD $\sim 2Dt$), while the green line shows a slope of 2, consistent with ballistic motion governed by equation 2.17. A discussion of the MSD for discrete time series is presented in Appendix A.

the macroscopic random steps. This manifests on the Log-Log graph by a slope greater than 1 (in fact, here as in true ballistic motion, the slope is 2). The inertial motion captured on these higher time resolutions suggests that it should be possible to observe ballistic motion in real particles.

The advent of tweezers has allowed a great deal of headway to be made in this area. Compared with previous investigations in bulk media [55–58], the direct observation of single particles has greatly improved the ability of experiments to directly measure positions and velocities. There are also more rigorous treatments, which apply higher order corrections to the equations of motion at very short timescales. These formulations also take into account hydrodynamic memory effects, stemming from the inertia of the fluid being displaced by the Brownian particle [59–61]. The work in references [59–61], initially arising from the observation of long time-tails in the velocity autocorrelation function [62–64], has led to some of the most precise measurements of Brownian motion [17].

Most investigations into such stochastic systems have centered upon the study of the PACF and the PSD [19], where the characteristic timescale on which Brownian motion transitions to ballistic motion is defined by the momentum relaxation time, $\tau_p = \frac{1}{\Gamma}$. Details of the kinematics on timescales much smaller than τ_p have been investigated by references [18, 20, 21] in both underdamped and overdamped regimes by direct computation of correlation functions. In comparison, numerous experiments to extract physical properties such as the color of the stochastic force [25], the viscosity of the fluid [27], the polarizability [29] and the mass of particles [35] have relied on measurements of the PSD.

Much of the work described above has involved the implementation of very fast quadrant detectors or differential photodiodes and fiber bundles, which due to their high bandwidth, have become the state-of-the-art [15]. This has led to such sensors replacing conventional direct imaging which has played a vital role in tweezers experiments since the inception of ODF laser traps [3]. However, with the recent availability of high-speed cameras, direct imaging has had a resurgence [65].

In order to observe ballistic Brownian motion, a direct imaging system requires a temporal resolution, or a frame rate, comparable to $1/\tau_p$. It is such an ultra-fast sensor that provides the necessary time resolution to perform the precise mass measurements that we describe in Chapter 4. As a result of the acquisition rates accessible to these types of cameras, in Section 4.1.3, we also present a brief demonstration of video microscopy with a fast CMOS sensor to observe the transition from ballistic to diffusive Brownian motion.

Since both the confining potential and the surrounding fluid play very little role in particle motion on this very short timescale, the MSD in the ballistic regime can be directly related to the kinetic energy of a Brownian particle.

We can define the mean-squared velocity of such a particle to be:

$$\begin{aligned}\langle v(t)^2\rangle &= \langle\left(\frac{x(t_0+t)-x(t_0)}{(t_0+t)-t_0}\right)^2\rangle \\ &= \frac{\langle(x(t_0+t)-x(t_0))^2\rangle}{t^2}\end{aligned} \tag{2.24}$$

and by using equation 2.15, we can relate this to the MSD:

$$\langle v(t)^2\rangle = \frac{\langle[\Delta x(t)]^2\rangle}{t^2}, \tag{2.25}$$

By invoking an alternate version of the equipartition theorem (equation 2.20), we can equate the kinetic energy of a particle in the ballistic regime with its thermal energy to write:

$$\begin{aligned}\frac{1}{2}m\langle v(t)^2\rangle &= \frac{1}{2}k_BT \\ \frac{1}{2}m\frac{\langle[\Delta x(t)]^2\rangle}{t^2} &= \frac{1}{2}k_BT,\end{aligned} \tag{2.26}$$

In this way, a measurement of the MSD, on a timescale of $t \ll \tau_p$, can be used to generate an initial estimate of particle mass.

Furthermore, since the momentum relaxation time can also be expressed as a function of the damping coefficient, $\tau_p = \frac{m}{\gamma}$, a simple measurement of τ_p can be combined with particle size measurements to make an alternate preliminary estimate of particle mass. In order to understand this second calculation, it is instructive to build up a quantitative understanding of the momentum relaxation time from more basic principles. Therefore, we digress in this next section to discuss an estimate of τ_p in the context of our free space experiments.

2.2.4 Comments on Viscosity

To estimate the timescale set by τ_p for our experiments, in room temperature ($T = 300$ K) air, we must find an expression to represent this damping coefficient, γ.

This problem is most easily tackled in the context of a Stokes' flow system, which is to say, a relatively stationary or resting fluid that responds to external forces instantaneously. In this regime, we can represent the damping on a sphere of radius r_s by invoking Stokes' drag coefficient, $\gamma = 6\pi\eta r_s$, where η is the dynamic viscosity of the fluid. However, the use of Stokes' law requires an expression for the viscosity of the fluid.

To this end, a simple approximation can be made on the basis of the equipartition theorem and the kinetic theory of gases where colliding particles are treated as hard spheres [66]. For this approximation, we define the viscosity to be the coupling parameter between the force on an object and the velocity of the fluid around it.

We begin with what is known as Newton's law of viscosity, which can be used to describe the flow of a fluid near a solid surface at a position y moving in the $\widehat{x}$ direction, as shown in Figure 2.7. Given this orientation, the flux of $\widehat{x}$-momentum computed along the $\widehat{y}$ direction, ϕ_{xy} is proportional to the fluid velocity gradient

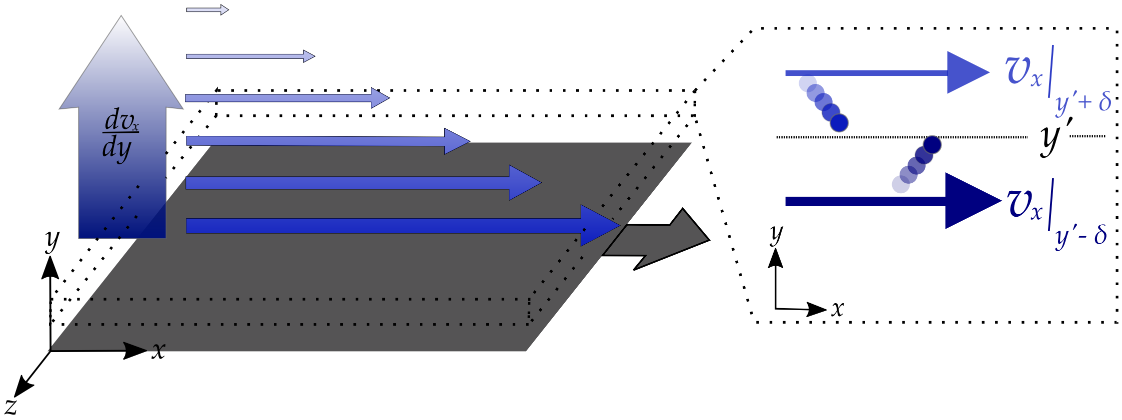

Figure 2.7: Demonstration of Newton's law of viscosity for a fluid near a solid surface. In this instance, the surface is in the xz-plane, moving in the positive $\widehat{x}$-direction, and generating a velocity gradient $\frac{dv_x}{dy}$ in the fluid along the $\widehat{y}$-direction. The inset shows the partitioning of space in the fluid about a given xz-plane (y'). The circles show fluid particles approaching y' with the velocities $(v_x|_{y'\pm\delta})$ that they obtained from their most recent collisions at $y' \pm \delta$.

along $\widehat{y}$; which is to say:

$$\phi_{xy} = -\eta \frac{dv_x}{dy} \tag{2.27}$$

where η is the coupling parameter called the viscosity.

We consider an otherwise non-interacting gas with a Maxwell-Boltzmann velocity distribution defined by an equilibrium temperature T. For the case of a gas with number density n, that is made up of spherical molecules of radius r_p and mass m_p, we can define an average speed of a gas molecule:

$$\overline{v} = \sqrt{\frac{8k_BT}{\pi m_p}}. \tag{2.28}$$

We can then also define the rate of collisions for such a gas per unit area of a stationary surface as:

$$Z = \frac{1}{4}n\overline{v} \tag{2.29}$$

and the mean free path as:

$$l = \frac{1}{\sqrt{32}\pi r_p n} \tag{2.30}$$

This allows us to partition a space of dimension $\delta = 2l/3$, near any xz-plane, where δ is the distance at which, on average, a gas molecule experiences its most recent collision before passing through the plane.

Then, as shown in the inset of Figure 2.7, we consider a gas flowing parallel to an xz-plane at position y' where the fluid velocity gradient is $\frac{dv_x}{dy}|_{y'}$. The net momentum passing through y' is then simply the difference between the momentum of particles travelling in each direction on either side of the plane:

$$\phi_{xy} = Zmv_x|_{y'-\delta} - Zmv_x|_{y'+\delta} \tag{2.31}$$

where we assume that each molecule is moving at the velocity it attained due to its most recent collision, which implies:

$$v_x|_{y'\pm\delta} = v_x|_{y'} \pm \delta\frac{dv_x}{dy} \tag{2.32}$$

Therefore, we can write the rate of momentum transfer as:

$$\begin{aligned}\phi_{xy} &= Zm(v_x|_{y'} - \delta\frac{dv_x}{dy} - (v_x|_{y'} + \delta\frac{dv_x}{dy})) \\ &= Zm(-2\delta\frac{dv_x}{dy}) \\ &= \frac{-1}{2}n\bar{v}m\delta\frac{dv_x}{dy}\end{aligned} \tag{2.33}$$

Comparing this with Newton's law of viscosity (equation 2.27), we can define the viscosity as:

$$\begin{aligned}\eta &= \frac{1}{2}n\bar{v}m\delta \\ &= \frac{1}{6r_p^2}\sqrt{\frac{k_BTm_p}{\pi^3}}\end{aligned} \tag{2.34}$$

While this treatment greatly simplifies the interaction between the molecules, it can be expanded to include the so-called Lennard-Jones potential to improve the accuracy of the prediction [66]. For nitrogen gas at room temperature ($m_p \sim 4.6 \times 10^{-26}$ kg and $r_p \sim 155$ pm) we can use equation 2.34 to estimate the viscosity as ~ 17 μPa·s, which is nearly the same as the empirical viscosity of air measured to be 18 μPa·s [67].

Thus by invoking Stokes' law to define the damping coefficient, we can show that

$$\begin{aligned}\tau_p =& 1/\Gamma \\ \tau_p =& m/\gamma \\ \tau_p =& m/(6\pi r_s \eta)\end{aligned} \tag{2.35}$$

where, r_s is the size of our particle. Which can easily be rearranged to define the particle mass as:

$$m = \tau_p 6\pi r_s \eta \tag{2.36}$$

Therefore, if we have an accurate measurement of the particle size, the observation of the transition from diffusive to ballistic motion can be used to infer a value of τ_p, which in turn can be used to derive a simple estimate for the mass of a trapped particle.

Similarly, in the reverse process, we can also make an estimate of the momentum relaxation time for a Brownian particle ($m \sim 10^{-13}$ kg and $r_s \sim 3$ μm) by again invoking Stokes' law to define the damping such that $\tau_p = m/(6\pi\eta r_s)$, which for air at room temperature air gives: $\tau_p \sim 100$ μs.

Using equation 2.35, this value of τ_p can also help estimate the level of damping for a constrained Brownian particle. Given a typical optical trap stiffness of $\kappa \sim 10^{-6}$ N/m, we can show that while $\Gamma^2 \sim 10^8$ Hz, the resonant frequency of the trap gives $4\omega_0^2$ only on the order of $\sim 10^7$ Hz, demonstrating the overdamped nature of the system described by equation 2.21.

From a practical standpoint, however, this value of τ_p also suggests the frame rates at which our experiments need to operate to capture the transition from ballistic to diffusive Brownian motion. Moreover, this calculation predicts the type of motion we should expect our particle to be undergoing at various time intervals.

To observe ballistic motion, the camera frame rate must be chosen such that the exposure time of a single frame is comfortably below this timescale. This also identifies the repetition rates that will ultimately be necessary in the drop-and-restore experiments, where the average of uncorrelated repetitions are needed to increase the signal-to-noise ratios of the trajectories.

2.3 Drop and Restore Kinematics

As mentioned at the outset, the mass determination technique that I have developed relies on averaging uncorrelated repetitions of particle motion during release and recapture from an ODF trap. The technique is underpinned by precise timing control of the turn-off and turn-on of the trapping potential using an AOM. We track a particle's trajectory as it is dropped from and subsequently restored to the equilibrium position in the ODF trap in two distinct measurements.

In the first of these experiments, the so-called "drop", the trapped particle is repeatedly released from the ODF trap. The motion of the particle falling in gravity

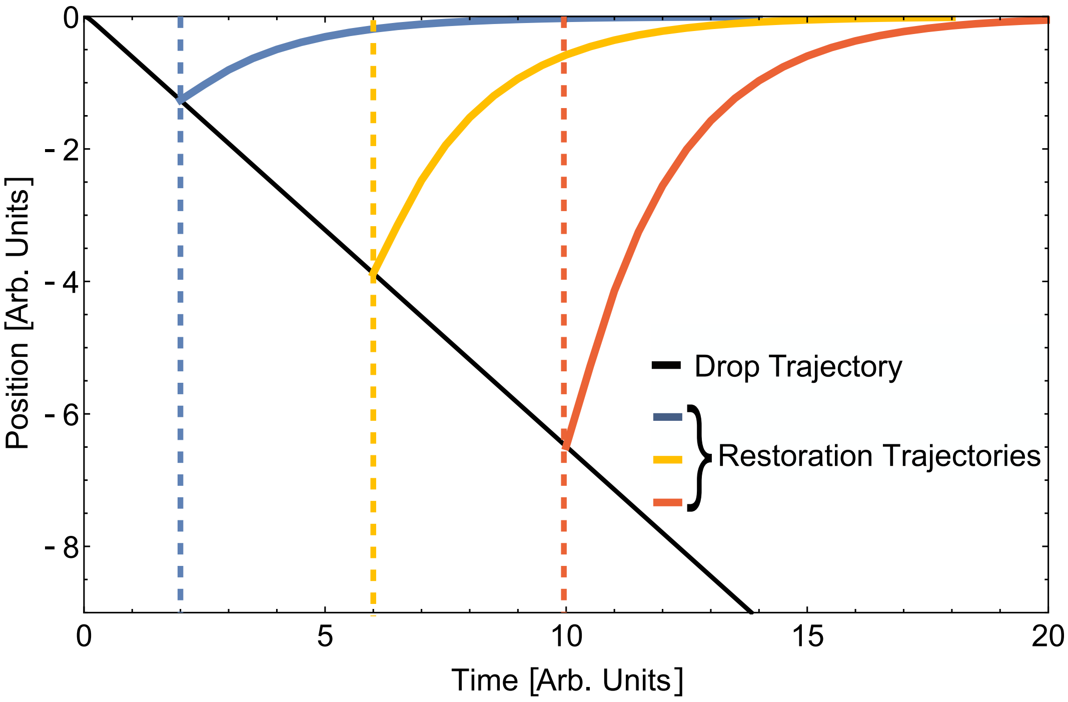

Figure 2.8: . Three restoration curves (solid lines modelled by equation 2.40) show the expected trajectory of a particle being restored to the equilibrium position in the ODF trap (position = 0) when the laser force is re-engaged after various drop times (dashed lines). The restorations begin with the expected recapture velocities and fall positions for a falling particle described by equation 2.38 with $v_r = 0$, as shown in black.

is modelled by:

$$\frac{\partial^2 x}{\partial t^2} + \Gamma \frac{\partial x}{\partial t} - g = A(t) \tag{2.37}$$

where $g = -9.8$ m/s^2 is the acceleration due to gravity in this coordinate system. Here, since we average uncorrelated repetitions, the stochastic driving term plays no role and the resulting solution to equation 2.37 is given by:

$$x(t) = \frac{g}{\Gamma}[t + (\frac{1}{\Gamma} + \frac{v_r}{g})(e^{-\Gamma t} - 1)] \tag{2.38}$$

as derived in Appendix B.1, where v_r represents the initial velocity of the released particle, which should average to zero over many uncorrelated repetitions. Consequently, a fit to the displacement-time graph of a falling particle can be used to extract the value of Γ. A visualization of the expected trajectory is shown in Figure 2.8.

In the subsequent experiment, the so-called "restore", when the laser confinement is turned on, the particle is restored, from its fallen position, to the trap center. This behavior is modelled by:

$$\frac{\partial^2 x}{\partial t^2} + \Gamma \frac{\partial x}{\partial t} + \omega_0^2 x - g = A(t). \tag{2.39}$$

Once again, since numerous uncorrelated restorations are averaged, the stochastic drive does not contribute to the effective solution of equation 2.39, which is given by:

$$x(t) = x_0 e^{\frac{-\Gamma}{2}t}[\cosh(bt) + \frac{\Gamma}{2b}\sinh(bt)] + \frac{v_0}{b}[e^{\frac{-\Gamma}{2}t}\sinh(bt)] \tag{2.40}$$

as shown in Appendix B.2, where, x_0 is the initial position and and v_0 is the recapture velocity, which is to say the velocity of the particle at the time when the laser force is turned on to initiate the restoration.

Combining all of these pieces, it is possible to infer the value of m from a fit to equation 2.40, using values of Γ from the drop experiments, and κ from independent measurements of the trap spring constant. By repeating the drop-and-restore over a range of drop times we are able to extract an even more precise value for the mass of the trapped particle. We show a theoretical illustration of several of these restoration trajectories, given an initial particle velocity of 0, in Figure 2.8.

Next, we comment on the expectations for the recapture velocity v_0 in equation 2.40. We note that for drop times $t \gg \tau_p$, v_0 can be estimated as the sum of the terminal velocity and the effect of the ODF during the first frame of exposure. The variation in the recapture velocity as a function of drop time can be modelled by

$$v_0(t_d) = v_T - t_{exp}\kappa x(t_d)/m, \tag{2.41}$$

where $v_T = \frac{g}{\Gamma}$ is the terminal velocity of the particle, t_{exp} is the exposure time for a single frame of acquisition, and $x(t_d)$ is the trajectory described by equation 2.38 as a function of drop time t_d.

Using equation 2.41, it is theoretically possible to reduce equation 2.40 to an expression where the particle mass is the only one free parameter. However, in order to more accurately model the observed motion of the particle, we leave both the recapturel velocity and the mass as free parameters. This means that we can extract both quantities (m and v_0) from our fits to equation 2.40. A discussion of the resulting trends in v_0 is presented in Section 4.2.

3 Experimental Details

3.1 Apparatus

The experiments were carried out with a homebuilt laser system operating at 780 nm, consisting of a master oscillator and semiconductor waveguide tapered amplifier (TA) placed on a pneumatically-isolated optical table. A schematic of the experimental set-up is shown in Figure 3.1. The power stability of the master oscillator has a characteristic Allan deviation of 5×10^{-6} at 10 s [68] and the TA has an output power of ~ 2 W [69]. The output of the TA was fiber coupled and gently focused through an AOM driven at 80 MHz so that the diffracted beam could be turned off or on in ~150 ns. As a result, it was possible to rapidly release the trapped particle in a gravitational field, and subsequently restore the particle to its equilibrium position. The turn-on and turn-off of the diffracted beam from the AOM were controlled by a pulse generator operated at repetition rates ranging from 0.5-20 Hz. The pulse width that defines the free-fall time of the particle is precise to the level of 1 ns. The maximum power in the diffracted beam (250 mW)

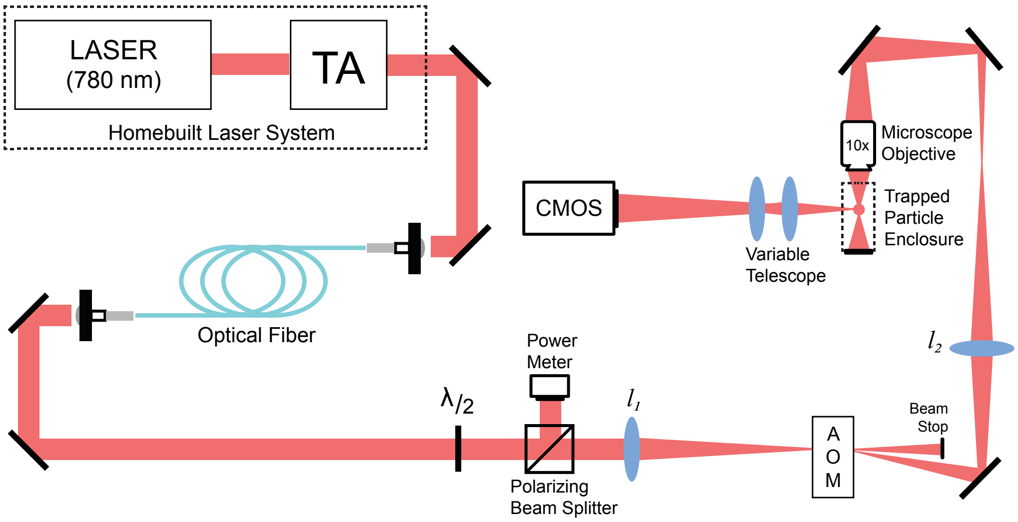

Figure 3.1: Schematic diagram of the experimental set up. The focal lengths of the beam shaping lenses are: $l_1 \sim 45$ cm and $l_2 \sim 30$ cm. The mirrors in between the acousto-optic modulator (AOM) and the 10× objective act as a periscope such that the beam entering the objective is directed downward along the vertical direction. Here TA represents the tapered amplifier, $\lambda/2$ represents a half-wave plate, and CMOS represents the camera.

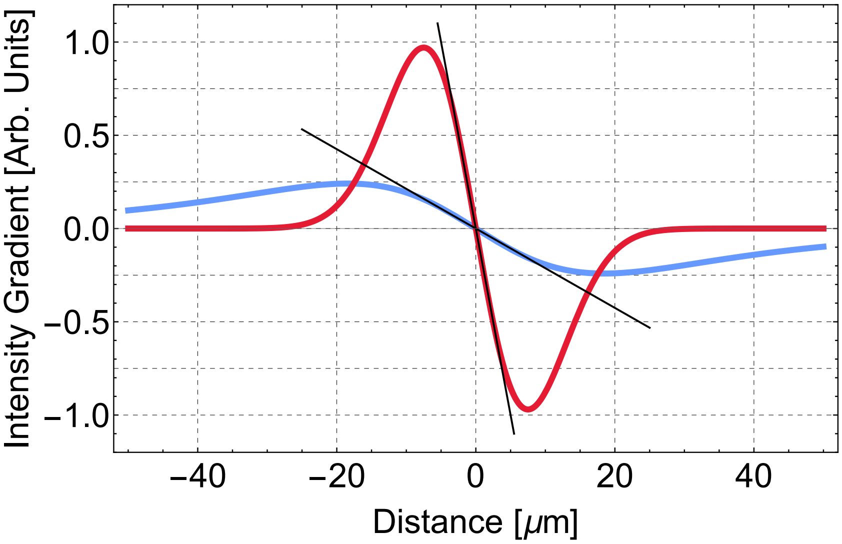

Figure 3.2: Intensity gradients along the vertical (light blue) and horizontal (red) directions. The straight lines indicate the linear (harmonic) ranges of the trapping potentials.

was controlled with a waveplate and polarizing cube beam splitter. The diffracted beam was expanded and focused through a 10× microscope objective (NA 0.25) so that the focus of the beam was ~ 5 mm from the end face of the objective lens. The intensity gradients associated with the ODF trap were characterized using a scanning knife edge spatial profiler as shown in Figure 3.2. The focal region was surrounded by a tightly-sealed enclosure with sliding glass windows to reduce air currents. In this free space configuration, the trapped particles were introduced by ablating from the tip of a permanent marker inserted into the enclosure. We note that this is a simple and effective technique for introducing particles into a free space optical tweezers set-up since the ablated particles have near zero velocity. Other techniques for introducing trapped particles are described in [3, 18, 19, 22, 70, 71]. The light scattered from the trapped particle in the transverse direction was imaged onto a CMOS sensor using a simple two-lens telescope with a variable magnification ranging from $\sim 40\times - 80\times$. The CMOS sensor (see Figure 3.3a) consisted of an 800×1280 pixel array with an overall size of 2.24 cm × 3.58 cm, which amounts to a pixel size of 28 μm. The camera was operated in continuous mode at a variable frame rate ranging from 1×10^4 to 2×10^5 frames per second (fps). The imaging system was calibrated by photographing a ruled micrometer slide placed in the object plane of the telescope. The calibration, as shown in Figure 3.3b, involved fitting the profiles of successive rulings in the image plane to Gaussians and deter-

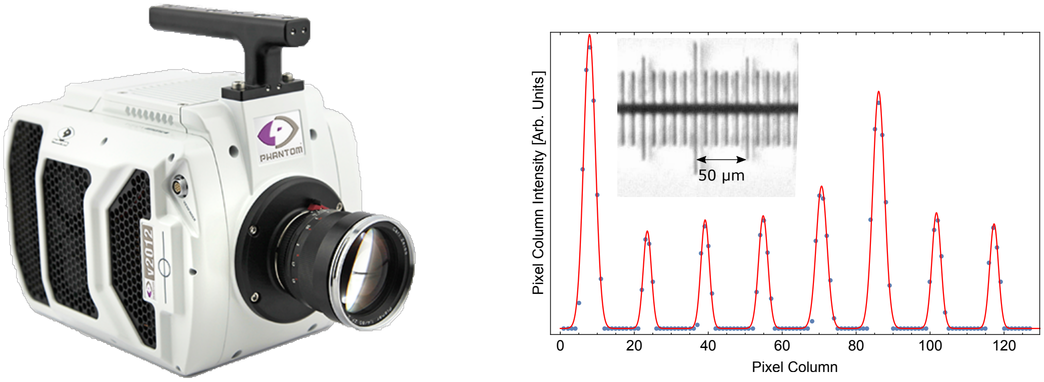

(a) (b)

Figure 3.3: (a) Phantom UHS-12 v2012 high speed camera, loaned from Delta Photonics for one week of measurements. Image acquired from reference [72]. (b) The total intensity per column of pixels across an image of a micrometer slide (shown as an inset) and Gaussian fits (red) to the rulings. This spatial calibration of the sensor area yields a conversion factor of 0.67 μm/pixel.

mining their separations in pixel units. Image sequences were stored in on-board memory and transferred to a computer for data processing. For the drop-and-restore experiments, 100 independent image sequences were averaged to improve the signal-to-noise ratio. In contrast, investigation of ballistic motion and PACF measurements relied on a continuous record length of images. To compensate for the lack of averaging in the PACF measurements, an intensity filter was used to reduce the effect of broadband background noise due to light entering the telescope.

3.2 Direct and Indirect Imaging

When measuring the kinematics of a trapped particle, one of the obvious first steps is to unambiguously determine the position of this particle, or target object. As I have outlined, there are two primary classes of identification, which I call direct and indirect imaging. In optical tweezers experiments, direct imaging normally employs a CCD or other sensor to capture images of the target particle. This can be done either with scattered light [38, 73] or by observing the shadow cast by the particle "down-stream" in the trapping beam path [54]. Indirect imaging involves the division of either down-stream or scattered light in at least two directions to generate a differential signal which reveals the position of the target image relative to the point of division. The classic example of this type of detection is a quadrant position detector (QPD) [51], but high-bandwidth set-ups have been realized using simple photodetectors and a light-dividing mirror [19].

Compared to indirect high-bandwidth detectors, such as differential photodiodes or fiber bundles, direct imaging on a CCD or CMOS sensor presents several advantages but also raises some additional challenges. One of the primary advantages is, of course, the ease of visualizing the target object. This luxury is often the reason that tweezers experiments frequently employ a direct imaging device in parallel with higher-bandwidth indirect detectors [74, 75].

The second main benefit of direct detection, is the simplicity of spatial calibration. Some common differential detectors require the rastering of a target object using a piezoelectric crystal, in order to calibrate the voltage read-outs of the devices [27, 51]. Similarly, split fiber bundles that are used to quantify three-dimensional motion of particles trapped in optical tweezers require detailed mapping of the spatial efficiency of the detector to have confidence in excursions of the particle (target object) from the center of the detector. Details of a version of this more precise form of calibration can be found in references [74, 75]. Conversely, direct imaging devices can often be calibrated simply by calculating the magnification of the imaging system and knowing the pixel size of the detector, or more rigorously by measuring the distance between calibrated rulings placed in the plane of the target object, as shown in Figure 3.3b.

A third benefit is the increased level of information provided by direct detection. This is because it is possible to extract the position, size, and shape of an object by processing a recorded image.

However, we must also note one of the short-comings of this approach, namely that it can only determine particle position within the target object plane and is (largely) insensitive to movements in the direction perpendicular to this plane. Often, a second direct imaging device is needed to image along the perpendicular direction. In contrast, more sophisticated indirect imaging techniques have been developed to allow a single detector to infer information about motion in all three dimensions [74]. It would seem that a similar approach could be taken with direct imaging but this has, to my knowledge, not been demonstrated.

Another challenge presented by direct imaging, is that the position of a target object is not immediately known upon acquisition of this image. The image must first be analyzed and the center of the target object must be “found”. This process of particle tracking is a field of research in and of itself. However, in this work, we utilized very simple tools which should be readily accessible to anyone setting up an optical tweezers experiment. Accordingly, we devote the next section to a discussion of the center-finding techniques which are used in the rest of this work.

3.2.1 Comments on Particle Tracking

A number of years ago, a large scale effort was undertaken to determine if a consensus could be found in terms of the most effective particle finding and tracking algorithm [76]. The results were expectedly mixed. However, it was established that the so-called center-of-mass (CoM) algorithms proved to be the fastest, while more comprehensive fitting routines proved slightly more accurate especially at higher signal-to-noise ratios. In reference [76], the task was broken down into two phases, identifying particles and linking trajectories. This is to say finding all of the particles in a given frame by discriminating against background noise and then

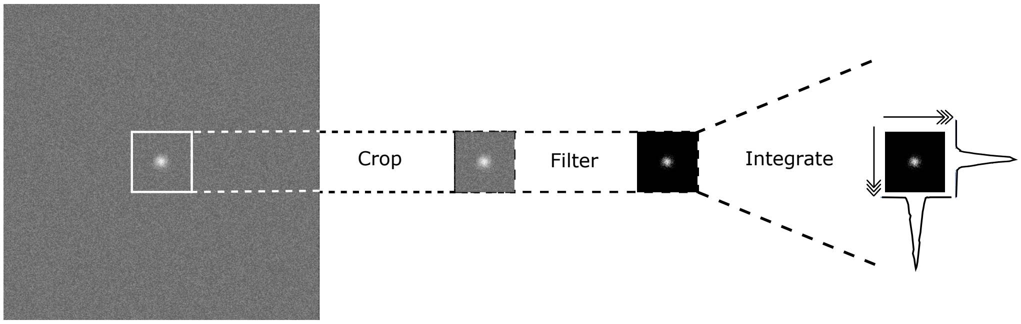

Figure 3.4: Schematic diagram of image processing sequence, whereby the initially acquired image is cropped around a region of interest, filtered with a cut-off threshold of pixel brightness, and then integrated along the two cardinal directions of the frame to generate particle profiles, which can be fit to extract position information.

determining which particle in a subsequent frame corresponded to each particle in the previous frame. Fortunately, in our case, and in the case of most tweezers experiments, single particle finding is the principal objective, which greatly reduces the complexity when compared to other forms of microscopy since there is no chance of confusing particles from frame to frame.

Instead of identification and linking, our techniques can be broken down into three distinct steps: (1) Region of Interest (ROI) selection (2) Image Filtration (3) Particle Location

Below, I briefly describe each of these steps, visualized in Figure 3.4, in greater detail.

ROI selection: This is the first step in our process. We crop the frame of the image to roughly 4-5 particle widths around the particle, which we identified as the brightest section of pixels in the frame. Since our particles were confined and, in general, moved across a span of only a few particle widths throughout observation, this cropping procedure could be done manually for each video, or even as the video was being recorded by restricting the active sensor size on the camera. For our drop-and-restore experiments, this procedure sometimes involved analyzing longer columns of pixels to encompass the full range of drop distances.

Image Filtration: Next, as the name would suggest, we imposed an intensity filter upon each of the images that we acquired based upon noise levels near the edges of a particular frame. This filter subtracted a stock pixel intensity value from all frames with a minimum final pixel intensity value allowed of 0. Rather than work in somewhat abstract pixel value units of our 12-bit camera resolution, our filtration system is characterized by a level number ranging from 0 to 15 that identifies the threshold as a fraction of the maximum pixel intensity in an average frame (see Table 3.1). After imposing this threshold filter on an acquired image, we then employed the last step of our center-finding procedure.

Table 3.1: Image processing threshold filter level legend. Table indicates the cut-off value, as a fraction of the maximum pixel value in a frame, at which pixels were identified as dark (i.e. set to 0) for the purposes of particle identification.

Filter Level		Threshold [Fraction of Maximum Pixel Intensity]	
0		0.000	
1		0.053	
2		0.107	
3		0.160	
4		0.213	
...		...	
13		0.694	
14		0.747	
15		0.800	

Particle Location: For our work, we concentrated on three primary techniques to identify the location of particles: (i) fitting pixel amplitude with a Gaussian function (ii) fitting pixel amplitude to a Sinc^4 function (iii) the employment of a CoM algorithm.

In general, both the Sinc and Gaussian methods were performed in the same manner. The pixels along the two cardinal directions of the frame were summed to generate a particle profile and the appropriate function was fit to this sum.

For the CoM algorithm, the same type of ROI was initially selected, and after summing along a direction, a weighted average was performed based upon the pixel column/row intensities to determine the center position. However, it has been noted that such conventional CoM algorithms have inherent bias that scales with the relative size of the ROI as compared to the target object [77]. To address this issue, our CoM-finding algorithm was augmented with a three-fold shrinking window similar to that recommended in reference [77]. Here, after initially finding the particle position by weighted average (CoM1), the ROI is reduced (by $\sim 1/2$) symmetrically about the implied center position. Then, a second weighted average was tabulated yielding a second position (CoM2), around which the ROI was again reduced for the third repetition, which ultimately yielded a final CoM position (CoM3).

In order to determine the most effective particle location technique to employ, we

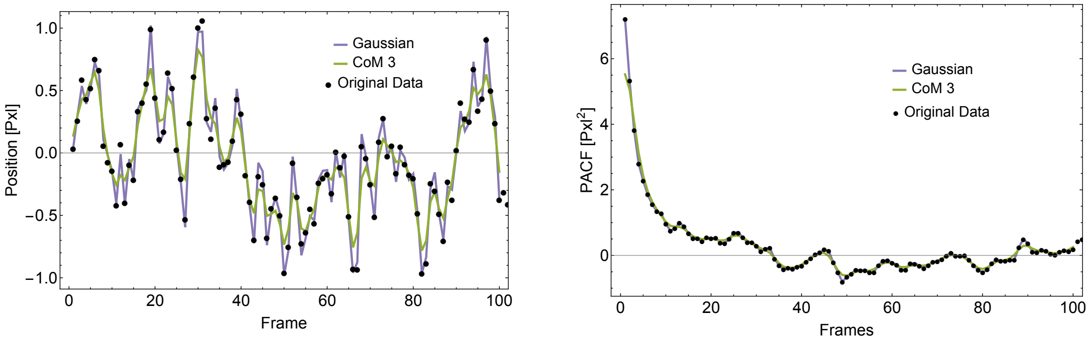

(a)

(b)

Figure 3.5: (a) Trajectory of a virtual random walker (black points) superimposed with the instantaneous position measurements made using Gaussian fitting and center-of-mass fitting algorithms. (b) PACFs calculated from 1000-frame samples of a virtual random walk and the instantaneous position measurements shown in part (a). All images have an image signal-to-noise ratio of 0.5 and an imposed intensity Filter Level of 10 (i.e. 0.6 times the maximum pixel intensity value).

tested each of these methods on a series of virtual Brownian particles. We generated images of such particles performing constrained random walks with various signal-to-noise ratios to identify any inherent noise or uncertainty associated with each protocol. Here, the signal-to-noise ratio was changed by adding white noise of increasing amplitude to the virtual Brownian particle images. A sample of one such virtual random-walk is shown in Figure 3.5a, along with the calculated trajectory from two of our fitting algorithms.

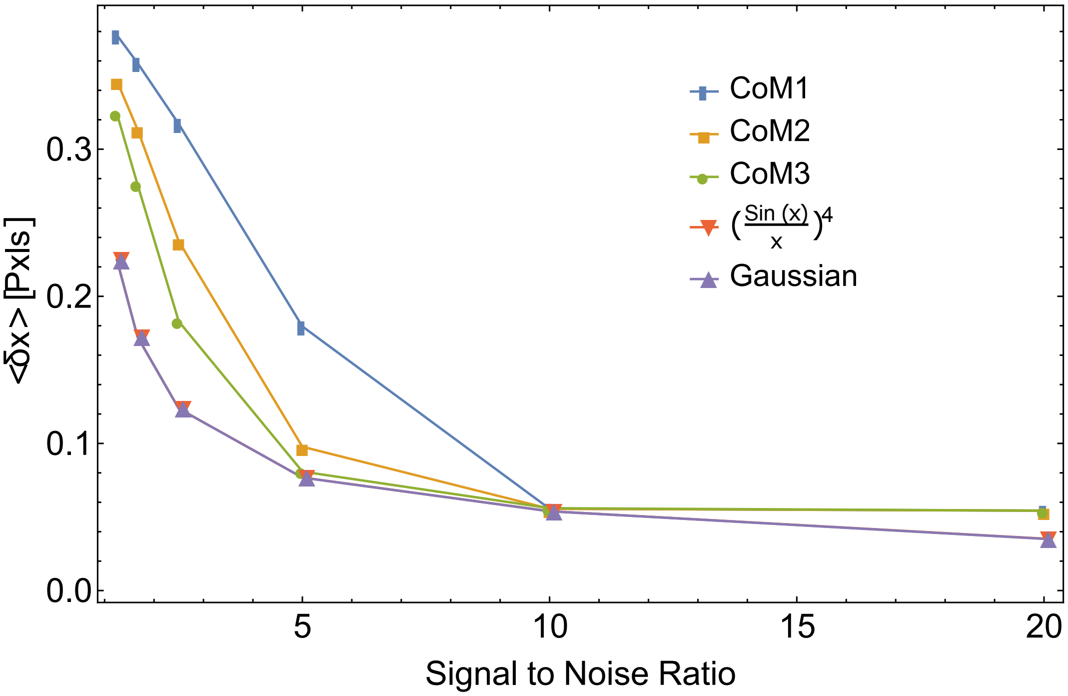

Figure 3.6: The average variance of various center finding algorithms as a function of background signal-to-noise ratio for 1000-frame random-walks of virtual particles. Here, CoM1 indicates a large window center-of-mass calculation, while CoM2 and CoM3 indicate the iterated CoM calculations with respectively shrinking ROIs. $(\frac{\sin x}{x})^4$ and Gaussian both represent routines which fit to integrated particle profiles.

All three routines perform qualitatively well and can be used to calculate PACFs based on equation 2.15 which are also quite accurate, as shown for the CoM and Gaussian techniques in Figure 3.5b. However, to quantify the effectiveness of each protocol, we calculated the variance of each algorithm relative to the positions of a virtual particle over walks consisting of 1000 frames (Figure 3.6).

Despite the three-fold nature of our CoM procedure, we still found (as alluded to in reference [76]) that CoM detection was the fastest of the three methods, and that it was highly competitive with fitting routines for images with high signal-to-noise ratios. We also found that the accuracy of our CoM began to break down at lower signal-to-noise ratios (see Figure 3.6). Given this, we largely employed the CoM method, particularly for the drop-and-restore measurements where sequence averaging ensured a higher signal-to-noise ratio. However, in order to extract particle size information and for frames with very short exposure or those which were identified to have a low signal-to-noise levels, the Gaussian fitting algorithm was prefered.

In general, with all three of our center finding algorithms, we found that the particle center could be tracked with an uncertainty of just under one tenth of a pixel ($\sim$ 40 nm at a magnification of 40×), which is comparable to other direct imaging work with tweezers [22, 41, 78] and represents the inherent uncertainty that we quote for our instantaneous position measurements.

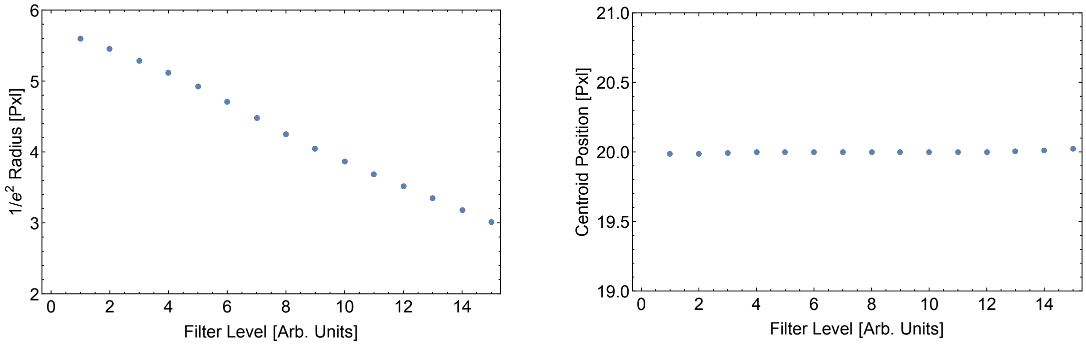

(a) (b)

Figure 3.7: (a) Effect of the imposed intensity filter on (a) the radius measured and (b) the measured centroid position of a virtual particle using a Gaussian fit to the particle profile.

Of note, we found no dependence of any of our center finders on the initial intensity filter that we applied, up to 0.8 of the maximum pixel value of a given frame. For filter levels larger than 0.8, we attribute the decrease in accuracy to insufficient signal. This is of importance in our discussion of autocorrelation functions (see Section 4.3). We further examine this effect in Figure 3.7, where we observe that while the radius of a particle identified with our center finders is affected by the filter level employed, both the accuracy of the position and the position itself were unaffected. We attribute this primarily to the fact that all of the expected intensity dependent effects (motional blur, pixel blooming, limited resolution etc.) are symmetric, meaning, for example in the case of motional blur, that the mean

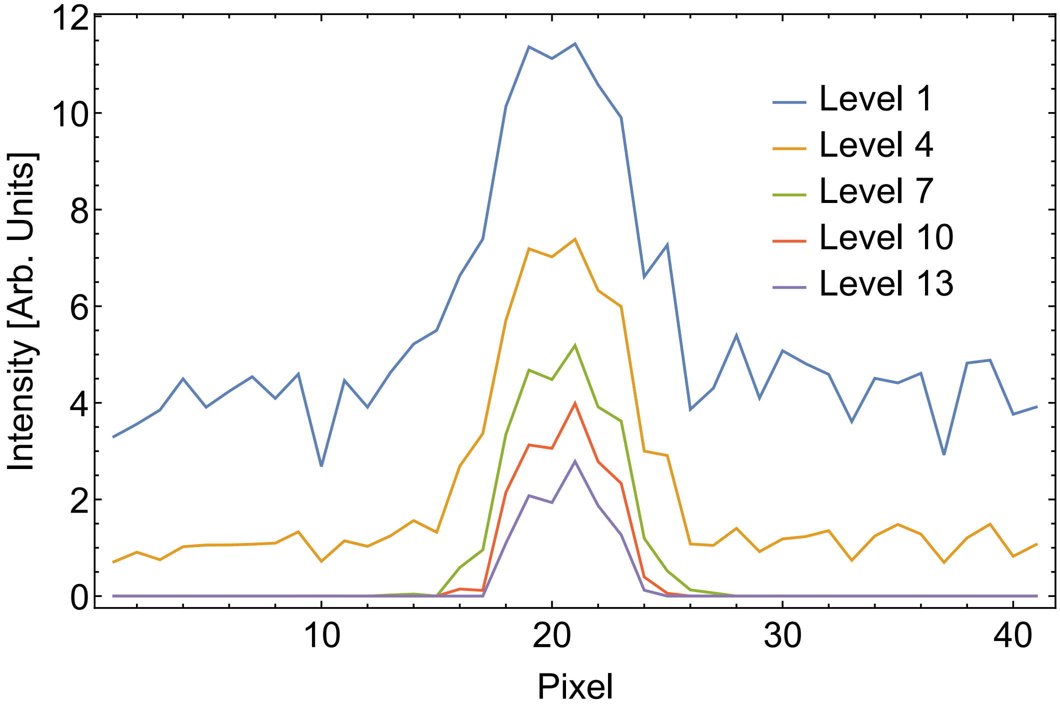

Figure 3.8: Particle profile as a result of intensity filtering. Here, each pixel represents the sum along a vertical column of pixels across the ROI and the levels indicate incremental steps in threshold from 0 (Level 1) up to 0.8 (Level 15) of the maximum pixel value in a frame.

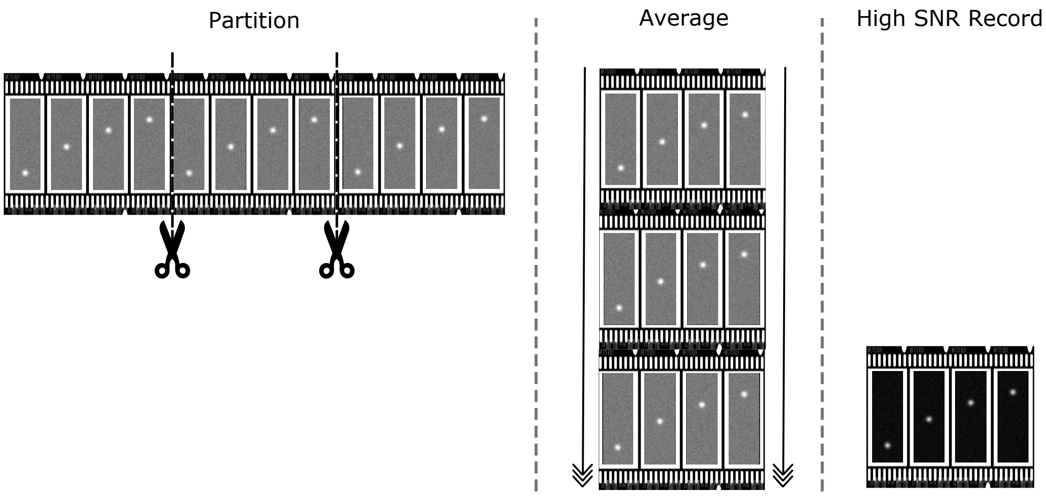

Figure 3.9: Schematic diagram of sequence averaging used for drop-and-restore measurements. Here, uncorrelated drop-and-restore frame sequences were partitioned and then averaged to increase the signal-to-noise ratio.

position of the particle would still have a maximum intensity at the same location with "dimmer wings" indicating the range of motion during the exposure time. Naturally, this should cause some intensity dependence in measurements of the radius, as the lower intensity"wings" are clipped (see Figure 3.8), but should leave the position or center of mass determination unchanged.

For the drop-and-restore experiments, there was an additional level of complexity to the position determination. Since uncorrelated iterations of the drops were performed and then averaged, the prescription for analysis became (1) ROI

Selection (2) Image Filtration (3) Sequence Averaging (4) Particle Location

In this new third step, all 100 iterations of a particular drop were partitioned and every frame for each timestamp $t_i = t_{recapture} + i$ (where $t_{recapture}$ indicates the time when the particle was first recaptured) were subsequently averaged to improve the signal-to-noise ratio before integration and particle location fitting. A visual representation of this process is shown in Figure 3.9. It is through this procedure that the effects of Brownian motion are effectively averaged over in the drop-and-restore experiments. As a result, the modified forms of equations 2.37 and 2.39 can be written as:

$$\frac{\partial^2 x}{\partial t^2} + \Gamma \frac{\partial x}{\partial t} - g = 0 \tag{3.1}$$

and

$$\frac{\partial^2 x}{\partial t^2} + \Gamma \frac{\partial x}{\partial t} + \omega_0^2 x - g = 0, \tag{3.2}$$

respectively.

4 Results and Discussion

In this chapter, I will outline the major experimental results of the thesis. These measurements, all made using video microscopy to observe micro-particles trapped in free space optical tweezers, consist of three main types: apparatus calibration, drop-and-restore mass measurements, and corroborating PACF-based mass measurements. While the latter two measurements can be explained based on the background in Chapter 2, the calibration measurements involve spatial determinations of particle size and measurements of the trap spring constant based on the equipartition theorem. Additionally, this chapter includes tests of short-time resolution and investigations into direct imaging of ballistic motion. We show that measurements of the MSD in the ballistic regime can be used to estimate the mass of micro-particles. Furthermore, we show that the capacity to detect the timescale at which the transition to ballistic motion occurs can be combined with measurements of particle size to provide an even simpler estimate for the mass of a trapped particle. These estimates are validated by the results of the drop-and-restore and

PACF based mass measurements. All of the results presented in this chapter are based on using the CoM3 particle finding technique (outlined in Chapter 3), with the exception of the discussion of particle size where the Gaussian fitting algorithm is employed to extract an intuitive particle radius.

4.1 Initial Measurements and Calibrations

4.1.1 Spring Constant Determination

Figure 4.1 shows the measurement of the spring constant of the ODF trap as a function of laser power. For each laser power, the spring constant was obtained from a Gaussian fit to the histograms of instantaneous positions (inset in Figure 4.1). The Gaussian fit has a functional form:

$$G(x) = Ce^{-\frac{\kappa x^2}{k_B T}} \tag{4.1}$$

where x is the instantaneous position and C is a normalization constant [51]. Equation 4.1 predicts that as κ increases, the spread in the instantaneous position (x^2) will decrease, due to the restriction imposed by equation 2.20.

Here, the particle positions were recorded with an exposure time of 10 μs on a suitably long timescale ($t \gg \tau_0$) to ensure uncorrelated measurements. This method of determining the trap spring constant is independent of measurements of the damping or the particle mass, in contrast with alternative approaches that

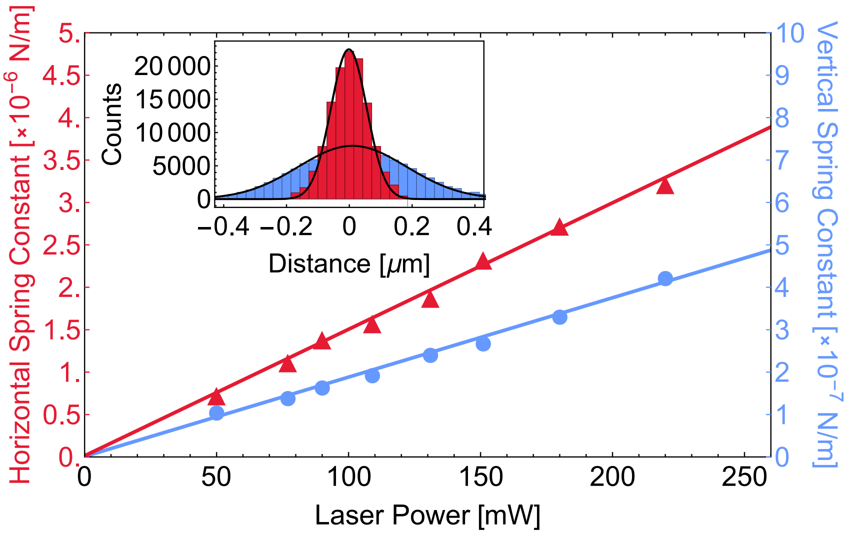

Figure 4.1: Trap spring constant as a function of laser power along the horizontal (left-red axis) and vertical (right-light blue axis) directions. The linear fits to the two data sets give $\kappa = [(1.49 \pm 0.04) \times 10^{-8}\ \frac{\mathrm{N/m}}{\mathrm{mW}}]\ P + [(1.36 \pm 5.61) \times 10^{-8}]$ N/m along the horizontal direction and $\kappa = [(1.87 \pm 0.07) \times 10^{-9}\ \frac{\mathrm{N/m}}{\mathrm{mW}}]\ P + [(1.11 \pm 4.16) \times 10^{-8}]$ N/m, along the vertical, where P is the laser power in mW. Inset shows examples of position histograms in the vertical (light blue bar) and horizontal (red bar) directions for a representative laser power (77.5 mW). The black lines show Gaussian fits to equation 4.1, whose widths are used to calculate the spring constants.

rely on the power spectrum [51]. From linear fits in Figure 4.1, we obtain spring constants of 1.49×10^{-6} N/m in the horizontal direction and 1.87×10^{-7} N/m in the vertical direction, for a typical laser power of 100 mW. We note that the offsets predicted by the fit equations in Figure 4.1, which are small, can be used to estimate the inherent noise in the detection system [54]. We also note that relative values of the spring constant in each direction is consistent with the relative magnitudes of intensity gradients along the same directions (see Figure 3.2). In all results that follow, the spring constant of the trap is varied by changing the laser power. We observe the behaviour of our optical tweezers to be highly consistent with an ODF trap and see no strong evidence to suggest any photophoretic component to the trapping forces acting on the resinous particles. Specifically, we see no consistent axial translation of the equilibrium position of the trap as the laser power is changed, a feature which has been closely tied to photophoretic trapping [32, 33, 79, 80].

4.1.2 Particle Size Estimation

One of the advantages of direct visualization is that, in addition to position, it should also provide information regarding the particle shape and size. While the CoM method was largely used in this work, the other two fitting routines provide more easily understandable metrics for the particle radius. For example, using our Gaussian fitting algorithm we can measure a $1/e^2$ radius for our particle to be

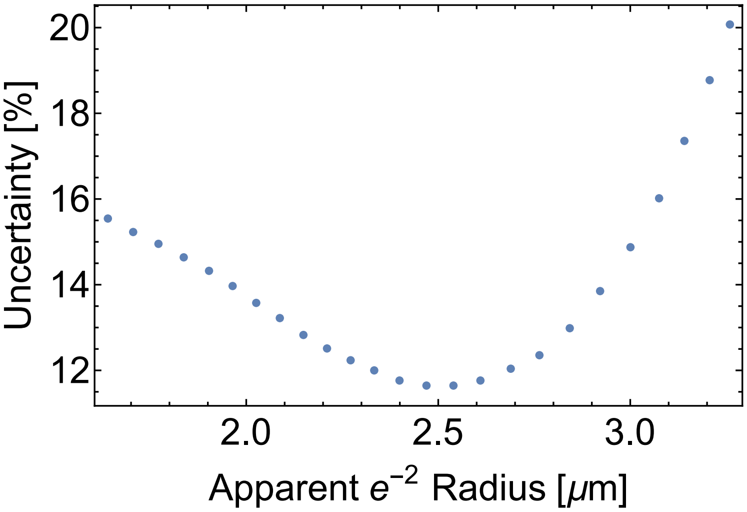

Figure 4.2: Uncertainty in the radius inferred from direct imaging using a Gaussian fit to the vertical particle profile as a function of the radius measured. Here, the radius was varied by changing the imposed intensity filter as in Figure 3.7.

2.5 ± 0.2 μm. However, the accuracy of this process is complicated by the fact that the particle in question is moving, even if in the limited way that constrained Brownian particles move.

Nevertheless, we can still make a reasonably good measurement of the particle size by examining images from our direct visualization. Here, we must address three distinct effects: (1) the absolute resolution of the camera including effects like pixel blooming, (2) motional blur in the target object plane, and (3) depth of field (DoF) infringement arising from motion perpendicular to the target object plane.

The first of these issues is quite tractable, but involves one subtlety. As explained in the Section 3.2.1, with respect to the center-finding algorithms that we employed, the first step was to impose an intensity filter across the entirety of the frame. We noted that the filter had essentially no effect on the particle position as shown in Figure 3.7b, but that the same could not be said for the particle radius, which reduced as the filter threshold level was increased (see Figure 3.7a). This can be explained by thinking of the particle's spread as a Gaussian, which as the threshold level is increased, begins to have its wings "clipped" to zero (see Figure 3.8), thereby influencing the veracity of the fit. To address this issue, we vary the filter level and record the resulting radius as well as the uncertainty in this radius as shown in Figure 4.2. Here, we take the minimum in the uncertainty to represent the filter level (level 6) at which the noise begins to dominate the measurement.

To address the case of motional blur, we perform another simple test, we increase the exposure time, averaging together a number of sequential frames and measure the change in radius as a function of exposure time. We then estimate what the particle radius would be at zero exposure time (i.e. an instantaneous measurement), as shown in Figure 4.3. This effect results in an average increase in the particle radius of ~ 15 nm for the exposure time of 10 μs used in our standard measurements.

To combat the third issue, we would ideally have a second camera to visualize the trap from the perpendicular direction and perform a similar motion blur

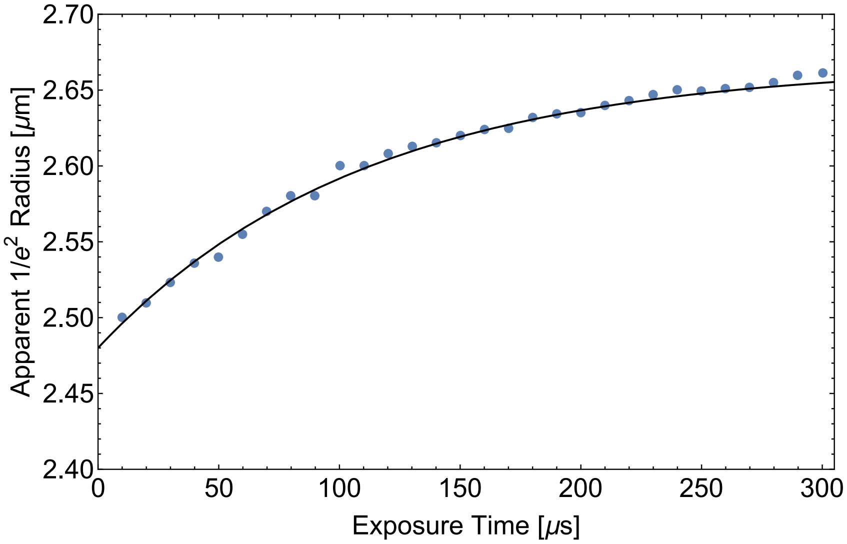

Figure 4.3: Inferred particle radius from Gaussian fits as a function of camera exposure time. Here, the exposure time was varied by averaging sequential frames. The black fit line is of the form $A(1-e^{-t/\tau_{exp}})+B$, with $A = 1.87$ μm, $B = 2.48$ μm, and $\tau_{exp} = 109$ μs.

Table 4.1: Summary of the corrections made to particle size determination from video microscopy.

Processing step	Particle radius	Correction
Initial (uncorrected) particle observation	3.25 μm	
Absolute resolution/Image filtration		-755 nm
Motional blur compensation		-15 nm
DoF excursions		-60 nm
Final determination	2.42 μm	

experiment. However, such a set-up was not at our disposal [1]. As such, we must first determine this DoF and understand how far our particle will move in and out of this field. Following reference [81], we can determine the DoF to be ~ 2 μm. Since the particle itself has a radius of ~ 2 μm, we should expect minor blurring on the basis of reference [81]. This expectation arises by comparing the DoF with the average motion of the particle in the radial direction. We find that the particle moves through a range of roughly 10% of the DoF. Accordingly, we approximate the blurring effect from this motion as $\sim$ 10% of the absolute resolution of the imaging system, ~ 0.06 μm, as estimated in reference [73].

---

[1] The key measurements presented in this thesis were completed over a period of one week by borrowing a single high-speed camera.

Combining all three of these relatively minor corrections, shown in Table 4.1, we can arrive at our best estimate for the particle radius of 2.4 ± 0.3 μm. We note that the final quoted uncertainty represents the size of half of a single camera pixel at the working magnification, and that this result was remarkably consistent across all of the resin particles observed as part of these investigations.

4.1.3 Brownian Motion Investigation

In Section 2.2.4, we calculated the momentum relaxation time for a 3 μm particle to be $\sim$ 100 μs. Since our imaging system is capable of acquiring images with exposure times of under 10 μs, we are able to demonstrate the capability to observe the onset of ballistic motion of optically trapped particles. We detect this onset as in Figure 2.6b, by recording the positions of a trapped particle and calculating the MSD. A discussion of MSD calculation for this type of discrete time series is presented in Appendix A.

As shown by equation 2.16, a measurement of the MSD is essentially identical to the construction of the PACF for the same time series. Figure 4.4 shows an observed MSD where we can see the characteristic behaviour of constrained Brownian motion. The MSD does not indefinitely scale a t^1 as in free diffusion (shown by the red line). Thus the slope deviates from the free diffusion value of 1 and tends to zero on long timescales.

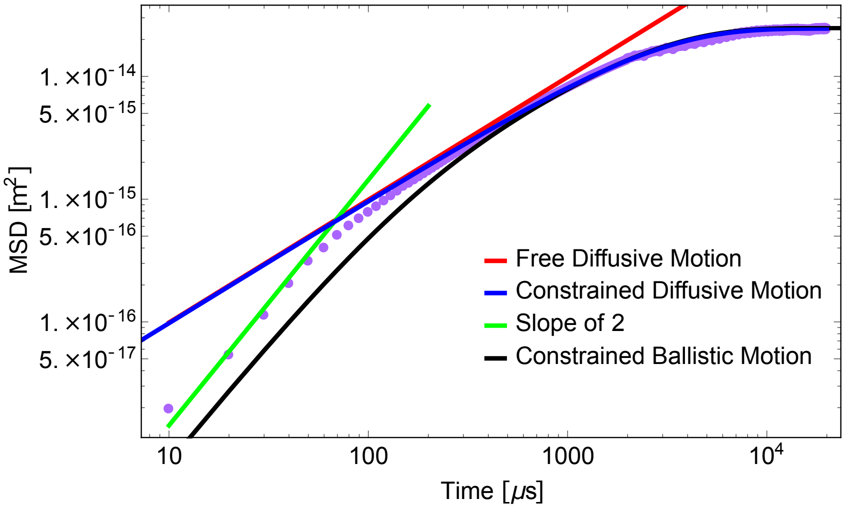

Figure 4.4: MSD of a confined resin particle. Images were acquired at 10^5 fps and with a trap spring constant of 3×10^{-7} N/m. The red line has a slope of 1, consistent with diffusive Brownian motion in the absence of a confining potential (equation 2.18). The blue line shows the theoretical MSD in the highly overdamped limit described by equations 2.16 and 2.23. The green line shows a slope of 2, consistent with ballistic motion, illustrating the slope of the short timescale measurements. The black line shows the theoretical predictions of constrained ballistic motion defined by equations 2.16 and 2.21. Each prediction assumes $\gamma = 8.38 \times 10^{-10}$ kg/s, $m = 5.5 \times 10^{-14}$ kg, and $\kappa = 3 \times 10^{-7}$ N/m.

On short timescales, where the motion is expected to transition to the ballistic regime, the MSD disagrees with the prediction based on equations 2.16 and 2.21. We attribute this discrepancy to insufficient time resolution leading to the inability of the MSD to simultaneously fit the behaviour on short and long timescales. This mirrors the difficulty described in Section 4.3, surrounding the modelling of PACFs using equation 2.21. The limitations posed by inadequate time resolution in analysing such data have been described in references [30] and [82].

Despite this shortcoming, we can still see a distinct change in the behaviour of the MSD, with the slope of 2 (green line) indicating non-diffusive Brownian motion. We can estimate the value of τ_p as $\sim 70\ \mu$s, where we observe a clear deviation from the slope of 1, indicative of the diffusive predictions. This inference agrees with our estimate, in Section 2.2.4, of $\tau_p \sim 100\ \mu$s. In addition to demonstrating the ability of the direct imaging setup to detect the transition from diffusive to ballistic motion, we can also use this data to obtain preliminary estimates of the particle mass.

Here, the relatively limited time resolution of the experiment presents a challenge for safely picking a timescale where $t \ll \tau_p$, in order to make a mass determination using equation 2.26. If, for example, we choose $t = 30\ \mu$s, then we only have $t \sim \tau_p/2$, which does not entirely satisfy the necessary limit. Nevertheless, taking the observed value of the MSD at 30 μs, we can use equation 2.26 to show:

$$\begin{aligned} m = & \frac{k_B T}{\langle [x(t)]^2 \rangle} t^2 \\ \sim & \frac{(1.38 \times 10^{-23} \ \frac{\mathrm{m^2kg}}{\mathrm{s^2K}}) \ 298 \ \mathrm{K}}{(1.13 \times 10^{-16} \ \mathrm{m}^2)} (30 \ \mu\mathrm{s})^2 \\ \sim & \ 3.5 \times 10^{-14} \ \mathrm{kg} \end{aligned} \tag{4.2}$$

However, since this estimate relies on the absolute value of the MSD at these short times, the overall accuracy of such a calculation may be somewhat questionable due to the limitations imposed by the time resolution. To gain a better understanding of this determination, we can estimate the associated uncertainty by calculating the variation in m corresponding to the average MSD inferred from $t = 25$ μs and $t = 35$ μs, which gives a value of $\delta m \sim 1.8 \times 10^{-14}$ kg, or roughly 50%. Thus, we can see that without improvements to the time resolution of our experiments, it is likely that this determination may only serve as an order of magnitude estimate for the particle mass.

Alternatively, the inferred value of τ_p from the data in Figure 4.4 can also be used to estimate the mass of the trapped particle on the basis of equation 2.36. If we invoke Stokes' law for the damping coefficient, as given by $\gamma = 6\pi\eta r_s$, where r_s is the radius of the particle measured in the previous section, we can estimate the mass of the trapped particle as

$$\begin{aligned} m =& \ \tau_p 6\pi r_s \eta \\ m \sim& \ (70\ \mu s)6\pi(2.4\ \mu m)(18\ \mu\text{Pa}\cdot\text{s}) \\ m \sim& \ 5.7\times10^{-14}\ \text{kg} \end{aligned} \tag{4.3}$$

with an uncertainty of $\delta m \sim 1.5\times10^{-14}$ kg, or roughly 25%, with a large portion of this uncertainty stemming from the particle size measurement discussed in Section 4.1.2.

Since this mass estimate, unlike the previous approach, only relies on observing a general trend in the MSD rather than on the absolute value of the function, the accuracy may be slightly more reliable than the determination in equation 4.2. However, the precision of the mass determination in equation 4.3 is ultimately limited by the qualitative nature of the estimation of τ_p.

When considering preliminary determinations, such as these, it is encouraging that they agree within their associated uncertainties, despite the relatively large magnitudes of the uncertainties themselves. Taken together, we can use these initial estimates to verify the validity of the two more rigorous experimental techniques for mass determination presented in this thesis, namely, the drop-and-restore method and the PACF-based measurements. The next sections describe these two measurement techniques in more detail.

4.2 Mass Determination from Drop-and-Restore Experiments

In this section, I present the results of the drop-and-restore experiments for mass determination. Here, all of the particle position data is the result of the four-step procedure outlined at the end of Chapter 3, using the CoM algorithm.

Figure 4.5a shows the position of the released particles as a function of "drop time" (i.e. the time after release from the trap). The position after each drop time is determined by averaging 100 individual uncorrelated repetitions. This free-fall data is fit to equation 2.38 to determine Γ, with a statistical uncertainty of $\sim$1%. Since the system is highly damped, the trajectory is dominated by the linear term in equation 2.38, the slope of which defines the terminal velocity v_T.

Figure 4.5b shows representative trajectories of particles that are being restored to the equilibrium position of the trap, after various drop times. The overall data collection time for a set of 13 drop-and-restore experiments was $\sim$ 90 seconds. The restoration trajectories are fit to equation 2.40 on the basis of known values for κ from the calibration (see Figure 4.1), as well as Γ and x_0 from the drop experiment (see Figure 4.5a). Combining all of these measurements, we are able to determine the mass of the falling particle from a two-parameter fit involving m and the recapture velocity v_0.

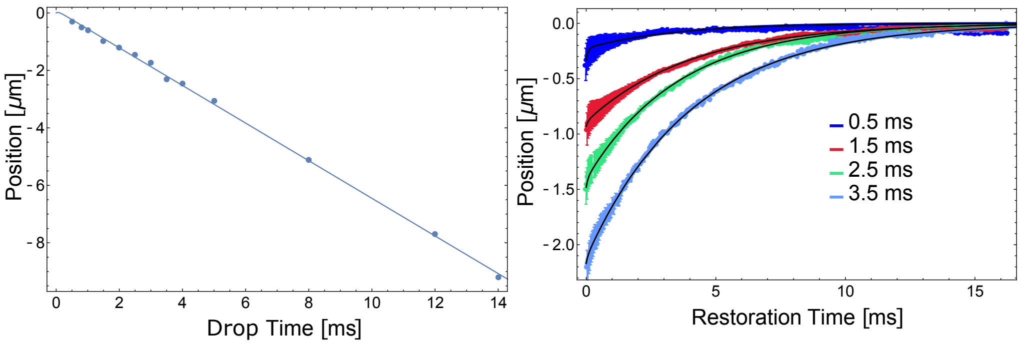

(a) (b)

Figure 4.5: (a) Shows the fall distance as a function of drop time and a fit to equation 2.38 with $\Gamma = 15.1 \pm 0.1$ kHz and $v_r = 0.7 \pm 0.5\ \frac{\mu\text{m}}{\text{ms}}$. (b) Shows the restoration trajectories along the vertical axis of the trapping beam, for a representative set of drop times. Fits to equation 2.40 are superimposed on the data in black. The spring constant for these restorations was $\kappa = 2.2 \times 10^{-7}$ N/m. The data for both the drop and the restore experiments represent averages of 100 independent repetitions and the error bars indicate the standard deviation of these repetitions. Here, we take the value of g to be -9.80 m/s^2.

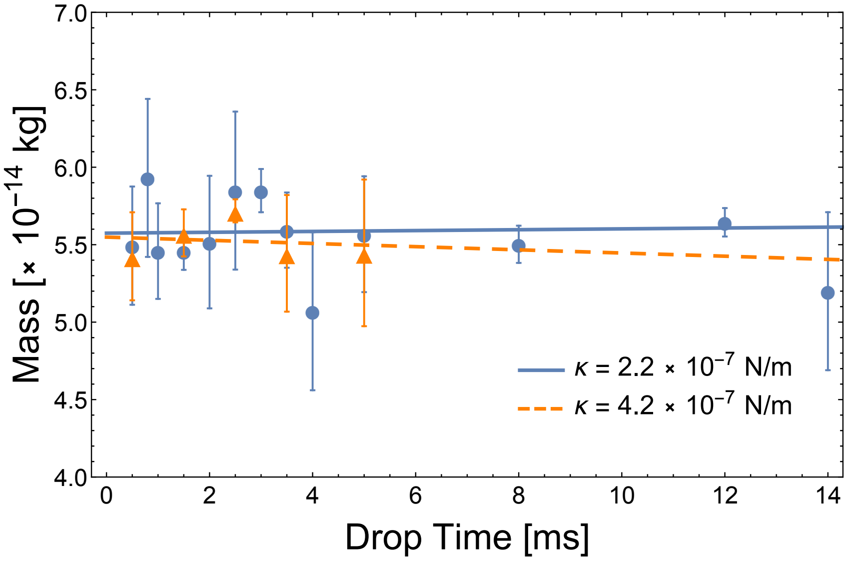

Figure 4.6: Mass determined using the drop-and-restore technique for various drop times. The restoration fits were performed using the values $\Gamma = 1.511 \times 10^4$ Hz from the drop experiment and $\kappa = 2.2 \times 10^{-7}$ N/m (circles) and $\kappa = 4.2 \times 10^{-7}$ N/m (triangles) from the vertical spring constant measurements. The fit line for $\kappa = 2.2 \times 10^{-7}$ N/m gives an offset value of $(5.58 \pm 0.08) \times 10^{-14}$ kg and a slope which is consistent with zero as expected, namely, $(2.74 \pm 9.86) \times 10^{-17}$ kg/ms. The fit line for $\kappa = 4.2 \times 10^{-7}$ N/m gives an offset value of $(5.55 \pm 0.12) \times 10^{-14}$ kg and a slope which is also consistent with zero, $(-1.1 \pm 4.0) \times 10^{-16}$ kg/ms.

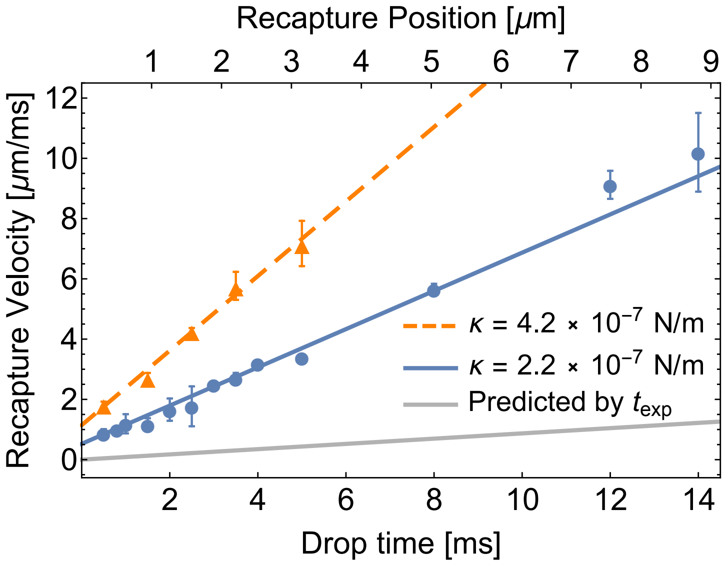

Figure 4.7: Fit values of v_0 from equation 2.40 as a function of drop time (lower axis) and recapture position with respect to the trap center (upper axis). The two horizontal axes are linearly dependent as described by the drop trajectory in Figure 4.5a. For $\kappa = 2.2 \times 10^{-7}$ N/m (circles), the solid fit line, which models the data as a function of drop time, gives an offset value of $v_0(t = 0) = (0.5 \pm 0.1)\ \frac{\mu\text{m}}{\text{ms}}$, and an acceleration given by the slope of $(0.63 \pm 0.03)\ \frac{\mu\text{m}}{\text{ms}^2}$. For $\kappa = 4.2 \times 10^{-7}$ N/m (triangles), the dashed fit line, which models the data as a function of the drop time, gives an offset value of $v_0(t = 0) = (1.2 \pm 0.2)\ \frac{\mu\text{m}}{\text{ms}}$, and an acceleration given by the slope of $(1.28 \pm 0.07)\ \frac{\mu\text{m}}{\text{ms}^2}$. The predicted value of the recapture velocity, also as a function of drop time, as defined by equation 2.41, is shown by the light gray trendline.

Figure 4.6 shows the mass extracted from the restoration trajectories for drop times ranging from 0.5 - 14 ms. The error bars represent the statistical uncertainty for each individual fit. For the 13 point data set (blue circles), corresponding to the drop times shown in Figure 4.5a, we find no systematic dependence on the drop time. From these measurements, we report a mass measurement of 5.58×10^{-14} kg, with a statistical uncertainty of 1.4%.

We estimate the overall uncertainty in m by numerically varying the parameters κ, Γ, and x_0 within experimental error, finding the statistical variation in m from the resulting trajectory fits, and combining these individual uncertainties in quadrature. In this manner, we infer a systematic uncertainty in m of 6×10^{-15} kg ($\sim 13\%$).

To further investigate the effect of trap stiffness, we repeated the drop-and-restore experiments for a subset of drop times, with a significantly larger ($\sim \times 2$) spring constant. We find that these mass measurements are consistent with those obtained with a smaller spring constant, as shown in Figure 4.6. Specifically, from these secondary measurements, we find a mass of 5.55×10^{-14} kg, with a similar statistical uncertainty of $\sim 2\%$, and once again, no systematic dependence of the mass on the drop time. This abbreviated study as a function of spring constant helps to demonstrate the insensitivity of the drop-and-restore technique to changes in the trap stiffness.

Figure 4.7 shows the fit values of the recapture velocity as a function of the

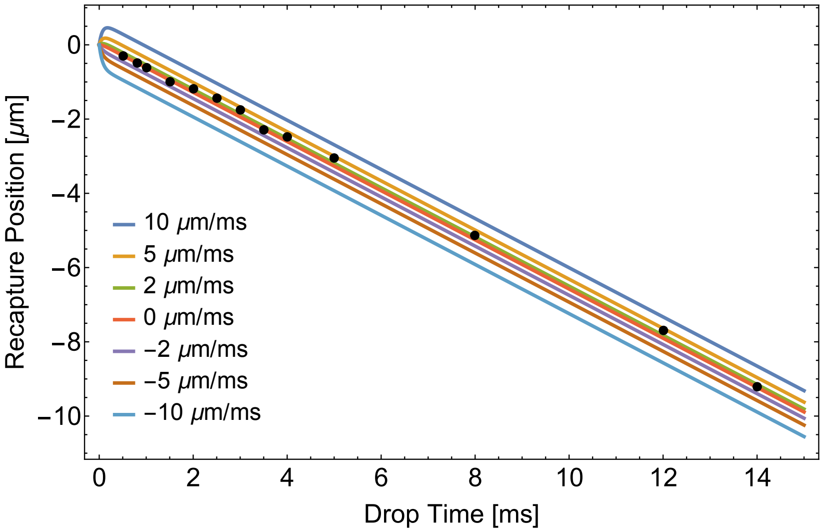

Figure 4.8: Drop data from Figure 4.5a in black, superimposed upon simulations of drop trajectories following equation 2.38 with various values of v_r.

drop time, for each of the mass determinations shown in Figure 4.6. The fit lines (dashed and solid) show that the initial recapture velocity continues to increase as the particle is allowed to fall further from the equilibrium position. Figure 4.7 also shows the predicted value of the recapture velocity, as defined by equation 2.41 (solid light gray line). We attribute the differences between the two trend lines and the prediction to an impulse proportional to the distance from the trap center imparted by the turn-on and -off of the AOM that produces a transient, uneven illumination of the particle.

Our conjecture is supported by the drop experiments, shown in Figure 4.5a, where the fit to equation 2.38 yields a small initial velocity, v_r. The data in Figure 4.5a suggests that there is a small impulse associated with the AOM turn-off since the measured fall distances agree with the predictions of equation 2.38, with a small release velocity. Figure 4.8 shows the extent to which a change in initial (release) velocity can alter the trajectory of a falling particle. Here, we note that the change in position calculated on the basis of equation 2.38 does not vary appreciably even for an initial (release) velocity that is double the value suggested by the fit in Figure 4.5a. Given these factors, we are confident that any impulse due to the AOM does not impact the mass determination.

Additionally, we note that the effect, indicative of a small impulse in the drop data, is consistent in magnitude with the offset extracted from the fit in Figure

4.7. This suggests that the same phenomenon could be responsible for both the release force and the short-drop restoration kicks. We propose that these features of the data arise because the resultant impulse imparted scales with distance from the beam focus (trapping zone) due to the position dependent nature of the ODF.

During the turn-off, or during the turn-on following a short drop time, the particle is near the uniformly illuminated region around the equilibrium position of the trap. In contrast, when the AOM is turned on after longer drop times, the particle is at increasing distances from the trap center where any uneven and transient illumination due to the AOM will have a larger effect. Therefore, the linear dependence of the recapture velocity on the drop time in Figure 4.7 can be attributed to the combined effects of the laser force, the impulse from the AOM, and gravity.

We also note that the recapture velocities measured with a higher trap spring constant exhibit a larger slope, as a function of drop time, in comparison to data obtained with a smaller spring constant. This behaviour further supports our conjecture that larger recapture velocities arise from the combination of a stronger laser force and the impulse from the AOM.

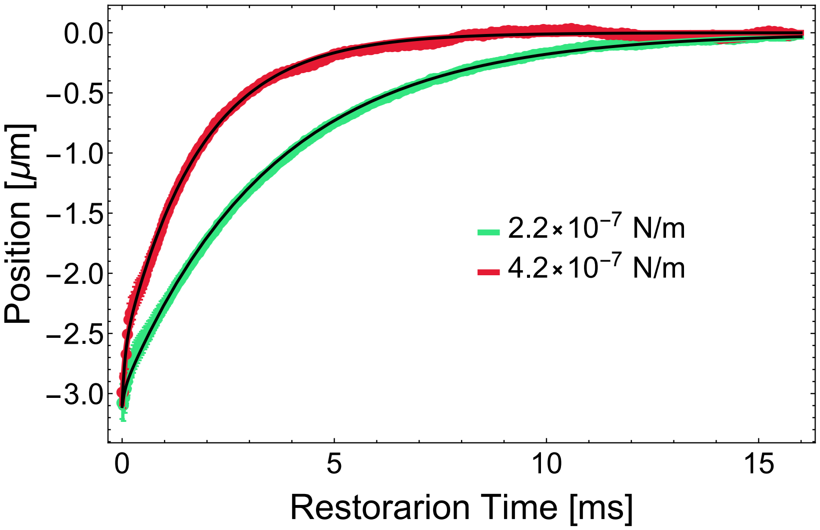

Figure 4.9: Restoration trajectories from a 5 ms drop for different spring constants. Fits to equation 2.40 are superimposed in black. The values of mass, recapture position, and initial recapture velocity are $(5.5 \pm 0.1) \times 10^{-14}$ kg, 3.43 ± 0.11 μm, and (7.4 ± 0.4) μm/ms for $\kappa = 4.2 \times 10^{-7}$ N/m and $(5.53 \pm 0.09) \times 10^{-14}$ kg, 3.50 ± 0.09 μm, and (2.7 ± 0.3) μm/ms for $\kappa = 2.2 \times 10^{-7}$ N/m.

4.2.1 Additional Trajectory Information

4.2.1.1 Spring Constant Effects

The conjecture that a small vertical kick is associated with the release of the particle is also supported by a closer examination of experiments in which the spring constant of the trap is varied. Figure 4.9 shows two restoration trajectories from 5 ms drops of the same particle with different trap spring constants. As expected, the restoration with a higher spring constant occurs on a more rapid timescale. Similarly, we note the proportional change in v_0 associated with increasing the spring constant of the trap, an effect which was qualitatively predicted in the simple model of equation 2.41. However, we also observe that the mass determinations and recapture positions extracted from the fits remain in agreement despite the disparity in laser power. These results highlight the trends in Figures 4.6 and 4.7, namely that the mass determinations obtained using the drop-and-restore technique are not sensitive to changes in the spring constant.

With that being said, from a practical standpoint, the effect of this more rapid initial velocity and shorter restoration period also mean that for the same acquisition frame rate, there are fewer points on the restoration curve with which the trajectory can be fit. While it may be possible to suppress impulses due to the turn-off and turn-on of the AOM using a double-pass configuration [83], the data also suggests that using a higher laser intensity will reduce the sensitivity of the technique in the configuration of the experiment that was used for this thesis.

4.2.1.2 Horizontal Trajectories

Since our apparatus employs direct imaging, we simultaneously acquire information about the horizontal trajectory of the particle during the drop-and-restore experiments. In an effort to better our understanding of the effect of trap stiffness and potential transient AOM-related forces, we examine trajectories in the horizontal direction. We show this in Figure 4.10, where we can see a consistently non-zero horizontal recapture position across many drop times. Each data point represents the horizontal co-ordinate of a released particle during the first frame of acquisition following turn-on of the trapping force. Like the vertical position measurements, these data also represent the average of 100 uncorrelated repetitions.

Although the horizontal displacement does not vary with drop time, it is clearly sensitive to changes in the spring constant of the trap. However, the extent of the change in the horizontal displacement can be anticipated based on the larger spring constant along this direction (see Figure 4.1). In attempt to quantify this effect, we solve a version of equation 2.37 for a damped particle given an initial velocity ($\frac{\partial x}{\partial t}(t = 0) = v_{x0}$) in the absence of any other external forces. The modified version

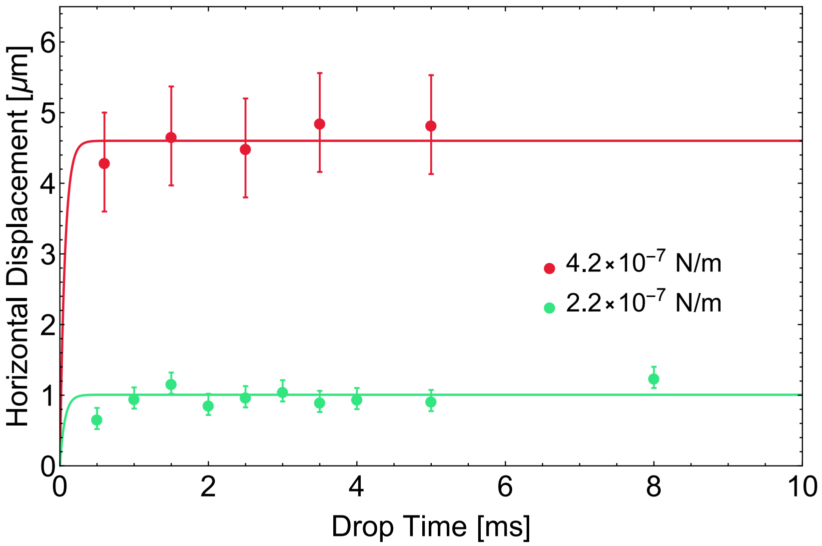

Figure 4.10: Initial horizontal displacement as a function of drop time for traps of different stiffness. Here, the trap spring constants indicate the value of the vertical trap stiffness, consistent with Figure 4.9. Fits to equation 4.5 are shown, which give an initial velocity value of (69 ± 1) μm/ms for $\kappa = 4.2 \times 10^{-7}$ N/m and (15 ± 1) μm/ms for $\kappa = 2.2 \times 10^{-7}$ N/m respectively. The error bars represent the standard deviation in the 100 independent repetitions which make up each data point.

of equation 2.37 can be written as:

$$\frac{\partial^2 x}{\partial t^2} - \Gamma \frac{\partial x}{\partial t} = 0 \tag{4.4}$$

which, given a release position of $x(0) = x_r$ and an initial velocity of $\frac{\partial x}{\partial t}(t = 0) = v_{x0}$, has the relatively simple solution:

$$x(t) = x_r + \frac{v_{x0}}{\Gamma}(1 - e^{-\Gamma t}) \tag{4.5}$$

Despite the fits to this function in Figure 4.10 showing behaviour consistent with an initial velocity imparted to the particle, it is unclear whether the trend in the data is exclusively the result of the turn-off or turn-on of the AOM. When compared to the vertical direction, we see a bigger effect in the horizontal direction that likely stems from the geometry of the beam relative to the AOM crystal, resulting in a more obvious uneven horizontal illumination during the rise and fall times of the AOM. This aspect could produce a much more pronounced and systematic impulse-related effect as the trapping beam “sweeps” on or off. It seems most likely that the effect that we see is the sum of a larger turn-off and turn-on kick than in the vertical direction, due both to the beam geometry and the greater spring constants in the horizontal direction (see Figure 4.1).

We also note another interesting feature of the data, namely a greater uncertainty in recapture positions when employing traps of higher spring constants (as shown by the error bars in Figure 4.10). This increasing level of positional uncertainty further supports the notion that using a higher laser intensity may ultimately reduce the sensitivity of the technique. We suggest that this spread is in fact the same type of statistical uncertainty present in the data corresponding to the vertical direction, but exacerbated by the more rapid speeds at which the particle is moving, as shown by the horizontal velocities extracted from fits to equation 4.5. Specifically, greater transient impulses from the AOM would lead to more motional blurring in the first frame of acquisition which would eventually begin to compromise the position measurement.

This uncertainty in the horizontal trajectory makes it more difficult to confidently extract information from these data sets. Nevertheless, further investigation appears worthwhile as more information about this horizontal impulse may lead to a more thorough understanding of the effects of amplitude modulating an ODF trap with an AOM and help shed light on the origin of the vertical impulses and any effect that they may have on the drop-and-restore experiments.

As mentioned in the previous section, we expect that the magnitude of these impulses can be significantly suppressed by employing a dual-pass AOM [83], or by using two synchronized AOMs oriented with counter-propagating sound waves to symmetrically shutter the trapping beam. We also anticipate that synchronization of the camera trigger with the AOM trigger will reduce the effect of motional blur and improve the measurements.

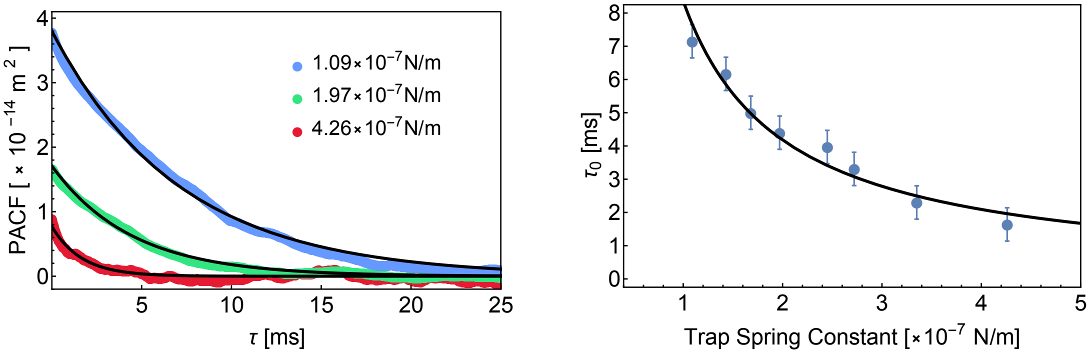

(a) (b)

Figure 4.11: (a) PACF of particle motion at various laser powers. The black lines show fits to equation 2.23, based on the overdamped approximation. Part (b) shows the resulting τ_0 from the PACF fits for a range of trap spring constants. The fit function is of the form $\tau_0 = \gamma/\kappa$, from which we obtain $\gamma = (8.38 \pm 0.23) \times 10^{-10}$ kg/s.

However, in order to further improve our confidence in the drop-and-restore technique, we examine another method for mass measurement, one that does not rely on amplitude modulating our trapping potential with an AOM. In the next section, I discuss the use of PACFs, developed in Chapter 2, to corroborate the mass determinations that we have presented thus far.

4.3 Mass Determination from Autocorrelation Functions

Figure 4.11a shows representative examples of PACFs, generated from data sets that are several seconds in duration with an exposure time of 10 μs (frame rate of

10^5 fps). This data, obtained at various laser powers, represents the time-domain analog of other techniques for mass determination that rely on measurements of the PSD [32, 35]. Here, however, the smoothness of the PACF suffers due to the record length, which was restricted to match that of the drop-and-restore experiments. While the PACFs can be fit to equation 2.21, the complex functional form results in an overestimate of the uncertainty in the mass. The large uncertainty persists even if the values of Γ and κ are constrained on the basis of independent experiments. To combat this, we model our data instead with the autocorrelation function in the large damping limit given by equation 2.23, since it has a much simpler functional form. Before doing so, however, we explicitly check the level of damping in our system to test the validity of this approximation.

By considering a typical trap spring constant, as determined in Section 4.1.1 ($\kappa = 2.2 \times 10^{-7}$ N/m) in combination with the damping rate ($\Gamma = 15.1$ kHz) and particle mass ($m = 5.58 \times 10^{-14}$ kg) measured in Section 4.2, we can show that $\Gamma^2 \sim 33(4\omega_0^2)$. This comparison not only demonstrates the decidedly overdamped nature of the ODF trap ($\Gamma^2 > 4\omega_0^2$), but also justifies the invocation of the large damping limit ($\Gamma^2 \gg 4\omega_0^2$) to describe our measurements. From the resulting fits to equation 2.23, we extract correlation time constants with a precision of approximately 3%.

Figure 4.11b shows the resulting fit values for the correlation time constant

Table 4.2: Summary of mass and particle size measurements based on various techniques. Here, ^{1} indicates the mass estimate made using equation 2.26 and the MSD at $t = 30\ \mu$s, while ^{2} represents the mass determination from the 13 drop-and-restore measurements taken with $\kappa = 2.2 \times 10^{-7}$ N/m. With reference to the PACFS, note that ^{3} indicates the mass determined by combining the time constants of PACFs in Figure 4.11b and the damping rate measured in drop experiments (Figure 4.5a), whereas ^{4} indicates particle size measurements inferred from Stokes' law using the same PACF time constants.

Mass determination		Particle size measurement	
Technique	Mass (kg)	Technique	Radius (μm)
Ballistic $\langle v(t)^2 \rangle$ ^{1}	$(3.5 \pm 1.8) \times 10^{-14}$	Direct Observation	2.4 ± 0.3
Inference of τ_p	$(5.7 \pm 1.5) \times 10^{-14}$		
Drop-and-restore ^{2}	$(5.58 \pm 0.08) \times 10^{-14}$	PACF & Stokes ^{4}	2.3 ± 0.1
PACF & Drop ^{3}	$(5.55 \pm 0.16) \times 10^{-14}$		

$\tau_0 = \gamma/\kappa$, as a function of trap spring constant (which is varied by adjusting the laser power). The error bars displayed in this figure represent the total uncertainty due to the intensity filter used to reduce the background noise in the PACFs and the inherent uncertainty in the exponential fits. This data, which exhibits the predicted inverse power dependence described in Chapter 2, can be used to extract a damping coefficient $\gamma = (8.38 \pm 0.23) \times 10^{-10}$ kg/s. Combining this result with the damping rate Γ measured in the drop experiments, we find a mass value of $(5.55 \pm 0.16) \times 10^{-14}$ kg, which corroborates the determination from the drop-and-restore experiments discussed earlier (see Table 4.2). Furthermore, we can see that both of these mass measurements are also in good agreement with the preliminary estimate of the particle mass made in Section 4.1.3 based on observations of τ_p.

The outlier with respect to mass determination, appears to be the estimate made using equation 2.26 and the MSD at $t = 30\ \mu$s, which just barely agrees with the two more rigorous determinations (drop-and-restore and PACF-based measurements) within a very large error bar. However, this discrepancy is almost certainly affected by the limited time resolution of our experiments and the questionable absolute accuracy of the MSD at the short times, as discussed in Section 4.1.3.

As another point of comparison, we can cross-check the experimentally determined values of τ_p for self-consistency. Here we can see that the drop experiments yield a value of $\tau_p = 1/\Gamma \sim 66\ \mu$s, which is consistent with the momentum relaxation time, $\tau_p = m/\gamma \sim 67$ μs, calculated using the combination of the mass from the drop-and-restore experiments (see Table 4.2) and the damping coefficient measured using the PACFs (see Figure 4.11b). We also note that both of these momentum relaxation time values are in broad agreement with the observed time constant, $\tau_p \sim 70$ μs, reported in Section 4.1.3.

Lastly, if we consider the same damping coefficient, extracted from Figure 4.11b, and assume Stokes' law, we can find the particle size to be (2.3 ± 0.1) μm. This is comparable to the radius inferred from images of the particle (2.4 ± 0.3 μm). As in Section 4.1.2, we note that this latter value, which is also shown in Table 4.2, takes into account the effects of calibration uncertainties such as absolute resolution, motional blurring, and DoF corrections. By combining this radius with the mass determined from the drop-and-restore experiments, we can infer a particle density of $(1.1 \pm 0.1)\times10^3$ kg/m^3, which is consistent with the density of resins used in common permanent markers [84].

5 Conclusions and Future Directions

The work presented in this thesis outlines simple and effective alternatives, compared to more elaborate conventional methods, for both visualizing trapped particles and measuring their masses and damping coefficients. Firstly, we have demonstrated the potential of direct imaging for observing short timescale Brownian motion in a simple apparatus and inferring masses of particles by detecting the transition to the ballistic regime. Secondly, we have presented a simple and effective technique based on drop-and-restore experiments in a gravitational field to determine the masses and damping rates of particles confined using free space optical tweezers. The mass determination, which has a statistical uncertainty of $< 2\%$, has been corroborated by position autocorrelation measurements, and is also in agreement with preliminary mass estimates based on ballistic Brownian motion observation (see Table 4.2).

In contrast with other techniques (see Table 1.1), our experiments do not require the use of secondary lasers, feedback systems, or vacuum environments. Instead, our measurements rely on direct imaging of scattered light with a fast CMOS sensor and a straightforward spatial calibration procedure.

We anticipate that the precision of this technique can be further improved by using higher laser powers and a larger Rayleigh range for the focused beam. This combination will increase the recapture range, defined by the turning points of the axial intensity gradient and allow the available field of view to be fully exploited. However, potential complications may arise from heating and local changes in the viscosity of the medium, which should be accounted for at higher laser intensities [37, 85, 86]. Additionally, we expect that the impulses attributed to the AOM can be significantly suppressed by employing a dual-pass AOM [83] and that the overall uncertainty in the measurement of initial velocities can be reduced by synchronizing the AOM and camera triggers to reduce the effect of motional blurring. It is also possible to further reduce the estimated systematic uncertainty by using faster frame rates to improve instantaneous position measurements. Similarly, the accuracy of spring constant measurements can be improved by actively stabilizing the power output of the AOM using an RF feedback loop and by using temperature-insensitive polarizers.

Our drop-and-restore method may also be used to study highly absorbing particles confined in photophoretic traps provided the effects of amplitude modulation in such traps are carefully modeled [32, 33]. Other extensions could involve the investigation of particulates trapped in liquids or media of higher viscosity. Based on the statistical precision, we expect that this technique should be applicable to the discrimination of contaminants in flue gases as well as biological agents such as pollen and pathogens trapped in free space and liquid cultures [79, 87–89]. Given the simplicity of the apparatus, the competitive precision, and the data acquisition time of approximately 90 s, we anticipate that this work will open the door for the rapid determination of relative masses for a variety of trapped particles in future studies.

Perhaps the most attractive feature of the drop-and-restore experiments is this versatility. While we tentatively propose its use in photophoretic traps, this protocol can easily be integrated into ODF experiments which employ alternative particle introduction methods, like those mentioned in Section 3.1 or with alternative imaging systems. The most promising untapped feature of this technique could be its integration with high-bandwidth indirect detection methods. The main limitation with the combination of the drop-and-restore technique with many indirect detectors is the more limited field of view due to the need for careful spatial calibration. However, if this were accomplished and the field of view were large enough to accomodate drops of significant duration, then such an apparatus would allow for both very short timescale investigation of Brownian motion and also ultra-precise measurements of the mass through observations of the drop-and-restore trajectories.

A Computation of MSD for Discrete Time Series

For a particular time-varying function $x(t)$, the MSD can be represented as a version of equation 2.15:

$$\langle[\Delta x(t)]^2\rangle = \langle(x(t') - x(t_0))^2\rangle \tag{A.1}$$

where, t' and t_0 are arbitrary time values separated by a time t. Thus, we can conceptualize the MSD as the average square difference of $x(t)$ at a particular time separation t.

For a discrete time series of M points, $x = \{x_0,\ x_1,\ x_2,\ ...,\ x_{M-1}\}$, the expectation value in equation A.1 can be replaced with a sum, such that the MSD becomes:

$$\langle[\Delta x]^2\rangle = \sum_{i=0}^{M-1-t} \frac{(x_{t+i} - x_i)^2}{M - t - 1} \tag{A.2}$$

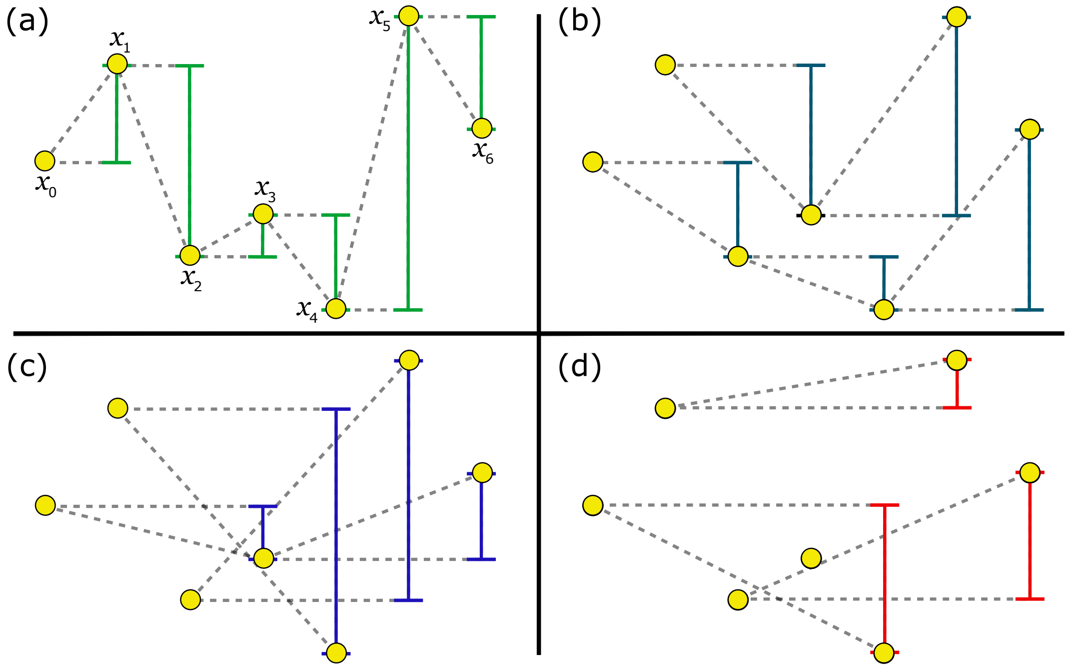

Figure A.1: Illustration of the differences used in the MSD calculation for a discrete time series x (yellow dots). Pairs of points separated by horizontally visualized timesteps: (a) $t = 1$, (b) $t = 2$, (c) $t = 3$, and (d) $t = 4$ are connected by dashed lines. The differences in x (shown as vertical separation) associated with these timesteps are indicated with solid lines.

Here, we can see that the MSD represents the average square difference of points in x at a particular time (index) separation t.

We note, that for a discrete time series, the MSD will show more variation from the continuous case as $t \to M$. In this limit, the sum in equation A.2 is a poor approximation for the expectation value in equation A.1. This is a consequence of there being fewer differences separated by $t \sim M$ in x to average together. An illustration of these types of differences is shown in Figure A.1 for an arbitrary time series. Due to the equivalence shown in equation 2.16, this dependence of the MSD on record length is mirrored in the PACF, as discussed in section 4.3. Practically, it is this condition which necessitates the acquisition of long record lengths in order to accurately compute both the MSD and the PACF.

B Derivation of Drop-and-Restore Trajectories

B.1 Drop Trajectory

We begin with equation 2.37, for a particle falling in gravity, which we will rewrite here as:

$$\frac{\partial^2 x}{\partial t^2} + \Gamma \frac{\partial x}{\partial t} - g = A(t) \tag{B.1}$$

Since the experiments rely on the average of uncorrelated repetitions, we take the expectation value of both sides, denoted by $\langle\ \rangle$. Due to the stochastic nature of $A(t)$, this reduces to equation 3.1, which we re-label:

$$\begin{gathered}\langle \frac{\partial^2 x}{\partial t^2} + \Gamma \frac{\partial x}{\partial t} - g \rangle = \langle A(t) \rangle \\ \frac{\partial^2 x}{\partial t^2} + \Gamma \frac{\partial x}{\partial t} - g = 0\end{gathered} \tag{B.2}$$

We can re-cast this equation, with a simple change of variables, to describe the particle velocity $v = \frac{dx}{dt}$:

$$\frac{\partial v}{\partial t} + \Gamma v - g = 0 \tag{B.3}$$

This first-order equation can readily be solved using separation of variables:

$$\begin{aligned} \int \frac{dv}{g - \Gamma v} &= \int dt \\ \frac{1}{\Gamma} \ln(g - \Gamma v) &= t + C \end{aligned} \tag{B.4}$$

where, C is a constant of integration.

From here we can easily solve for $v(t)$:

$$v(t) = \frac{1}{\Gamma}(g - Ae^{-\Gamma t}) \tag{B.5}$$

where, $A = e^C$ can be defined in terms of the initial velocity $v(0) = v_r$ such that $A = g - \Gamma v_r$.

By returning to the original variables, we can show:

$$\begin{aligned} \frac{\partial x}{\partial t} &= \frac{1}{\Gamma}(g - Ae^{-\Gamma t}) \\ \frac{\partial x}{\partial t} &= \frac{1}{\Gamma}(g - (g - \Gamma v_r)e^{-\Gamma t}) \end{aligned} \tag{B.6}$$

By using separation of variables again, we are able to find an expression for the position $x(t)$:

$$\int dx = \int \frac{1}{\Gamma}(g - (g - \Gamma v_r)e^{-\Gamma t})dt$$

$$x(t) = \frac{g}{\Gamma}t + \frac{g - \Gamma v_r}{\Gamma^2}e^{-\Gamma t} + B \tag{B.7}$$

$$x(t) = \frac{g}{\Gamma}t + (\frac{g}{\Gamma^2} - \frac{v_r}{\Gamma})e^{-\Gamma t} + B,$$

where B is another integration constant.

If we consider the equilibrium position of the trap to be $x(0) = 0$, then we arrive at the expression: $B = \frac{v_r}{\Gamma} - \frac{g}{\Gamma^2}$.

This then leaves:

$$x(t) = \frac{g}{\Gamma}[t + (\frac{1}{\Gamma} + \frac{v_r}{g})(e^{-\Gamma t} - 1)] \tag{B.8}$$

which is the solution given by equation 2.38.

B.2 Restoration Trajectory

For this derivation, we begin with equation 2.39, that models the motion of a particle being restored to the equilibrium position of an ODF trap. We rewrite this description as:

$$\frac{\partial^2 x}{\partial t^2} + \Gamma\frac{\partial x}{\partial t} + \omega_0^2 x - g = A(t). \tag{B.9}$$

Once again, since the restoration experiments rely on the average of uncorrelated repetitions we take the expectation value of both sides:

$$\langle\frac{\partial^2 x}{\partial t^2} + \Gamma\frac{\partial x}{\partial t} + \omega_0^2 x - g\rangle = \langle A(t)\rangle. \tag{B.10}$$

which reduces equation B.10 to equation 3.2, identified here as:

$$\frac{\partial^2 x}{\partial t^2} + \Gamma\frac{\partial x}{\partial t} + \omega_0^2 x - g = 0 \tag{B.11}$$

To solve this inhomogeneous linear equation, we must first find the complementary solution $x_c(t)$, by solving the homogeneous equation:

$$\frac{\partial^2 x}{\partial t^2} + \Gamma\frac{\partial x}{\partial t} + \omega_0^2 x = 0 \tag{B.12}$$

B.2.1 Finding $\mathbf{x_c(t)}$

Assuming a solution proportional to e^{kt}, for some constant k, we can show that equation B.12 can be written as:

$$e^{kt}(k^2 + \Gamma k + \omega_0^2) = 0 \tag{B.13}$$

which, since $e^{kt} \neq 0$, yields the characteristic polynomial:

$$k^2 + \Gamma k + \omega_0^2 = 0 \tag{B.14}$$

with roots:

$$k_{\pm} = -\frac{\Gamma}{2} \pm \frac{1}{2}\sqrt{\Gamma^2/4 - \omega_0^2} \tag{B.15}$$

For the overdamped case, which is to say $\Gamma^2/4 > \omega_0^2$, we have two real roots and a resulting solution of the form:

$$\begin{aligned} x_c(t) &= c_1 e^{k_+ t} + c_2 e^{k_- t} \\ x_c(t) &= e^{-\frac{\Gamma}{2}t}(c_1 e^{+\frac{1}{2}\sqrt{\Gamma^2/4-\omega_0^2}t} + c_2 e^{-\frac{1}{2}\sqrt{\Gamma^2/4-\omega_0^2}t}) \end{aligned} \tag{B.16}$$

Next, we must find a particular solution to equation B.11, $x_p(t)$, using the method of undetermined coefficients.

B.2.2 Finding $\mathbf{x_p(t)}$

Since the inhomogeneity in equation B.11 is an n^{th} order polynomial with respect to t ($n = 0$), we can use a particular solution that is also an n^{th} order polynomial:

$$\begin{aligned} x_p(t) &= a_0 t^0 \\ &= a_0 \end{aligned} \tag{B.17}$$

Using this, we can then calculate the derivatives of the polynomial a_0:

$$\begin{aligned} \frac{dx_p(t)}{dt} &= \frac{d}{dt}a_0 \\ &= 0 \end{aligned} \tag{B.18a}$$

$$\begin{aligned} \frac{d^2x_p(t)}{dt^2} &= \frac{d^2}{dt^2}a_0 \\ &= 0 \end{aligned} \tag{B.18b}$$

which we can then substitute into equation B.11 as the particular solution (equation B.17) to show:

$$\begin{aligned} \frac{\partial^2x_p(t)}{\partial t^2} + \Gamma\frac{\partial x_p(t)}{\partial t} + \omega_0^2x_p(t) - g = 0 \\ (0) + \Gamma(0) + \omega_0^2a_0 - g = 0 \\ a_0 = \frac{g}{\omega_0^2} \end{aligned} \tag{B.19}$$

The full solution to B.11 is then the sum of the general solution (equation B.16) and the above particular solution:

$$\begin{aligned} x(t) = x_c(t) + x_p(t) &= c_1e^{k_1t} + c_2e^{k_2t} + \frac{g}{\omega_0^2} \\ &= e^{-\frac{\Gamma}{2}t}(c_1e^{+bt} + c_2e^{-bt}) + \frac{g}{\omega_0^2} \end{aligned} \tag{B.20}$$

with $b = \frac{1}{2}\sqrt{\Gamma^2 - 4\omega_0^2}$.

Here, we note that the addition of the $x_p(t)$ only results in a constant offset to the complete solution, which represents the shifting of the equilibrium position of the trap due to gravity. Accordingly, we can redefine our co-ordinate system, like we did for equation B.8, so that $x = 0$ represents the equilibrium position. This means that in order to find a complete solution to the problem, we need only solve equation B.16 by finding the unknown coefficients c_1 and c_2.

B.2.3 Finding $\mathbf{x(t)}$

To complete the calculation and solve equation B.16, we first take $x(0) = x_0$ in order to find our first bounding value:

$$\begin{aligned} x_0 = x(0) &= e^{\frac{\Gamma}{2}(0)}(c_1e^{+b(0)} + c_2e^{-b(0)}) \\ &= c_1 + c_2 \end{aligned} \tag{B.21}$$

Next, in pursuit of a second boundary condition, we take the derivative of $x(t)$:

$$\begin{aligned} v(t) = \frac{\partial}{\partial t}x(t) &= \frac{\partial}{\partial t}e^{-\frac{\Gamma}{2}t}(c_1e^{+bt} + c_2e^{-bt}) \\ &= \frac{-\Gamma}{2}e^{\frac{-\Gamma}{2}t}(c_1e^{+bt} + c_2e^{-bt}) + be^{-\frac{\Gamma}{2}t}(c_1e^{+bt} - c_2e^{-bt}) \\ &= e^{\frac{-\Gamma}{2}t}[\frac{-\Gamma}{2}(c_1e^{+bt} + c_2e^{-bt}) + b(c_1e^{+bt} - c_2e^{-bt})] \end{aligned} \tag{B.22}$$

We can then use this and define the initial velocity v_0:

$$\begin{aligned} v_0 = v(0) &= e^{\frac{\Gamma}{2}(0)}(\frac{-\Gamma}{2}(c_1e^{+b(0)} + c_2e^{-b(0)}) + b(c_1e^{+b(0)} - c_2e^{-b(0)}) \\ &= c_1(b - \frac{\Gamma}{2}) - c_2(b + \frac{\Gamma}{2}) \end{aligned} \tag{B.23}$$

Plugging in the result from equation B.21, we have:

$$\begin{aligned} v_0 &= (x_0 - c_2)(b - \frac{\Gamma}{2}) - c_2(b + \frac{\Gamma}{2}) \\ &= x_0(b - \frac{\Gamma}{2}) - c_2(b - \frac{\Gamma}{2}) - c_2(b + \frac{\Gamma}{2}) \\ &= x_0(b - \frac{\Gamma}{2}) - 2bc_2 \end{aligned} \tag{B.24}$$

which then yields:

$$\begin{aligned} c_2 &= \frac{x_0}{2b}(b - \frac{\Gamma}{2}) - \frac{v_0}{2b} \\ &= x_0(\frac{1}{2} - \frac{\Gamma}{4b}) - \frac{v_0}{2b} \end{aligned} \tag{B.25}$$

and, in combination with equation B.21, gives:

$$\begin{aligned} c_1 &= x_0 - [x_0(\frac{1}{2} - \frac{\Gamma}{2b}) - \frac{v_0}{2b}] \\ &= x_0(\frac{1}{2} + \frac{\Gamma}{4b}) + \frac{v_0}{2b} \end{aligned} \tag{B.26}$$

By substituting B.25 and B.26 into equation B.16 we arrive at the full solution:

$$\begin{aligned} x(t) &= e^{-\frac{\Gamma}{2}t}[c_1 e^{+bt} + c_2 e^{-bt}] \\ &= e^{-\frac{\Gamma}{2}t}[(x_0(\frac{1}{2} + \frac{\Gamma}{4b}) + \frac{v_0}{2b})e^{+bt} + (x_0(\frac{1}{2} - \frac{\Gamma}{4b}) - \frac{v_0}{2b})e^{-bt}] \end{aligned} \tag{B.27}$$

which we can re-group to read:

$$\begin{aligned} x(t) &= e^{-\frac{\Gamma}{2}t}[(x_0(\frac{1}{2} + \frac{\Gamma}{b}) + \frac{v_0}{4b})e^{+bt} + (x_0(\frac{1}{2} - \frac{\Gamma}{2b}) - \frac{v_0}{2b})e^{-bt}] \\ &= x_0[\frac{1}{2}(e^{+bt} + e^{-bt}) + \frac{\Gamma}{4b}(e^{+bt} - e^{-bt})] + \frac{v_0}{2b}(e^{+bt} - e^{-bt}) \end{aligned} \tag{B.28}$$

and rewrite again using the Euler relations to be:

$$x(t) = x_0[\cosh(bt) + \frac{\Gamma}{b}\sinh(bt)] + \frac{v_0}{b}\sinh(bt)) \tag{B.29}$$

which is precisely the result described by equation 2.40.

C Research Contributions

C.1 Publications

Technique for rapid mass determination of airborne microparticles based on release and recapture from an optical dipole force trap, **G. Carlse**, K. B. Borsos, H. C. Beica, T. Vacheresse, A. Pouliot, J. Perez-Garcia, A. Vorozcovs, B. Barron, S. Jackson, L. Marmet, and A. Kumarakrishnan, Physical Review Applied, 14, 024017 (2020).

C.2 Conference Presentations

Optical tweezers experimen with home built laser systems, K. B. Borsos, **G. Carlse**, H. C. Beica, J. Perez-Garcia, A. Pouliot, T. Vacheresse, L. Marmet, and A. Kumarakrishnan, York University NSERC USRA Conference, Toronto, August 2019.

Bibliography

[1] G. Carlse, K. B. Borsos, H. C. Beica, T. Vacheresse, A. Pouliot, J. Perez-Garcia, A. Vorozcovs, B. Barron, S. Jackson, L. Marmet, and A. Kumarakrishnan. Technique for rapid mass determination of airborne micro-particles based on release and recapture from an optical dipole force trap. *Physical Review Applied*, 14(2):024017, 2020.

[2] A. Ashkin and J. M. Dziedzic. Stability of optical levitation by radiation pressure. *Applied Physics Letters*, 24(12):586–588, 1974.

[3] A. Ashkin and J. M. Dziedzic. Optical levitation of liquid drops by radiation pressure. *Science*, 187(4181):1073–1075, 1975.

[4] A. Ashkin and J. M. Dziedzic. Optical levitation in high vacuum. *Applied Physics Letters*, 28(6):333–335, 1976.

[5] A. Ashkin. Acceleration and trapping of particles by radiation pressure. *Physical Review Letters*, 24(4):156, 1970.

[6] A. Ashkin, J. M. Dziedzic, J. E. Bjorkholm, and S. Chu. Observation of a single-beam gradient force optical trap for dielectric particles. *Optics Letters*, 11(5):288–290, 1986.

[7] K. L. Corwin, S. J. M. Kuppens, D. Cho, and C. E. Wieman. Spin-polarized atoms in a circularly polarized optical dipole trap. *Physical Review Letters*, 83 (7):1311, 1999.

[8] N. Davidson, H. J. Lee, C. S. Adams, M. Kasevich, and S. Chu. Long atomic coherence times in an optical dipole trap. *Physical Review Letters*, 74(8):1311, 1995.

[9] A. Ashkin, K. Schütze, J. M. Dziedzic, U. Euteneuer, and M. Schliwa. Force generation of organelle transport measured in vivo by an infrared laser trap. *Nature*, 348(6299):346–348, 1990.

[10] B. N. Slama-Eliau and G. Raithel. Three-dimensional arrays of submicron particles generated by a four-beam optical lattice. *Physical Review E*, 83(5): 051406, 2011.

[11] R. E. Sapiro, B. N. Slama, and G. Raithel. Bragg scattering and Brownian motion dynamics in optically induced crystals of submicron particles. *Physical Review E*, 87(5):052311, 2013.

[12] T. T. Perkins, D. E. Smith, R. G. Larson, and S. Chu. Stretching of a single tethered polymer in a uniform flow. *Science*, 268(5207):83–87, 1995.

[13] F. M. Fazal, D. J. Koslover, B. F. Luisi, and S. M. Block. Direct observation of processive exoribonuclease motion using optical tweezers. *Proceedings of the National Academy of Sciences*, 112(49):15101–15106, 2015.

[14] C. Cecconi, E. A. Shank, F. W. Dahlquist, S. Marqusee, and C. Bustamante. Protein-DNA chimeras for single molecule mechanical folding studies with the optical tweezers. *European Biophysics Journal*, 37(6):729–738, 2008.

[15] I. Chavez, R. Huang, K. Henderson, E-L. Florin, and M. G. Raizen. Development of a fast position-sensitive laser beam detector. *Review of Scientific Instruments*, 79(10):105104, 2008.

[16] J. P. Staforelli, E. Vera, J. M. Brito, P. Solano, S. Torres, and C. Saavedra. Superresolution imaging in optical tweezers using high-speed cameras. *Optics Express*, 18(4):3322–3331, 2010.

[17] R. Huang, I. Chavez, K. M. Taute, B. Lukić, S. Jeney, M. G. Raizen, and E-L. Florin. Direct observation of the full transition from ballistic to diffusive Brownian motion in a liquid. *Nature Physics*, 7(7):576, 2011.

[18] T. Li, S. Kheifets, D. Medellin, and M. G. Raizen. Measurement of the instantaneous velocity of a Brownian particle. *Science*, 328(5986):1673–1675, 2010.

[19] T. Li and M. G. Raizen. Brownian motion at short time scales. *Annalen der Physik*, 525(4):281–295, 2013.

[20] B. Lukić, S. Jeney, Ž Sviben, A J. Kulik, E-L. Florin, and L. Forró. Motion of a colloidal particle in an optical trap. *Physical Review E*, 76(1):011112, 2007.

[21] B. Lukić, S. Jeney, C. Tischer, A J. Kulik, L. Forró, and E-L. Florin. Direct observation of nondiffusive motion of a Brownian particle. *Physical Review Letters*, 95(16):160601, 2005.

[22] D. R. Burnham, P. J. Reece, and D. McGloin. Parameter exploration of optically trapped liquid aerosols. *Physical Review E*, 82(5):051123, 2010.

[23] R. Di Leonardo, G. Ruocco, J. Leach, M. J. Padgett, A. J. Wright, J. M. Girkin, D. R. Burnham, and D. McGloin. Parametric resonance of optically trapped aerosols. *Physical Review Letters*, 99(1):010601, 2007.

[24] N. B. Viana, M. S. Rocha, O. N. Mesquita, A. Mazolli, P. A. Maia Neto, and H. M. Nussenzveig. Towards absolute calibration of optical tweezers. *Physical Review E*, 75(2):021914, 2007.

[25] T. Franosch, M. Grimm, M. Belushkin, F. M. Mor, G. Foffi, L. Forró, and S. Jeney. Resonances arising from hydrodynamic memory in Brownian motion. *Nature*, 478(7367):85, 2011.

[26] E. Hebestreit, M. Frimmer, R. Reimann, and L. Novotny. Sensing static forces with free-falling nanoparticles. *Physical Review Letters*, 121(6):063602, 2018.

[27] C. Guzmán, H. Flyvbjerg, R. Köszali, C. Ecoffet, L. Forró, and S. Jeney. In situ viscometry by optical trapping interferometry. *Applied Physics Letters*, 93 (18):184102, 2008.

[28] M. Grimm, T. Franosch, and S. Jeney. High-resolution detection of Brownian motion for quantitative optical tweezers experiments. *Physical Review E*, 86 (2):021912, 2012.

[29] P. Purohit, A. Samadi, P. M. Bendix, J. J. Laserna, and L. B. Oddershede. Optical trapping reveals differences in dielectric and optical properties of copper nanoparticles compared to their oxides and ferrites. *Scientific Reports*, 10 (1):1–10, 2020.

[30] K. Berg-Sørensen and H. Flyvbjerg. Power spectrum analysis for optical tweezers. *Review of Scientific Instruments*, 75(3):594–612, 2004.

[31] K. Berg-Sørensen, E. J. G. Peterman, T. Weber, C. F. Schmidt, and H. Flyvbjerg. Power spectrum analysis for optical tweezers. ii: Laser wavelength dependence of parasitic filtering, and how to achieve high bandwidth. *Review of Scientific Instruments*, 77(6):063106, 2006.

[32] J. Lin, J. Deng, R. Wei, Y-Q. Li, and Y. Wang. Measurement of mass by optical forced oscillation of absorbing particles trapped in air. *Journal of the Optical Society of America B*, 34(6):1242–1246, 2017.

[33] G-H. Chen, L. He, M-Y. Wu, and Y-Q. Li. Temporal dependence of photophoretic force optically induced on absorbing airborne particles by a power-modulated laser. *Physical Review Applied*, 10(5):054027, 2018.

[34] C. P. Blakemore, A. D. Rider, S. Roy, A. Fieguth, A. Kawasaki, N. Priel, and G. Gratta. Precision mass and density measurement of individual optically levitated microspheres. *Physical Review Applied*, 12(2):024037, 2019.

[35] F. Ricci, M. T. Cuairan, G. P Conangla, A W. Schell, and R. Quidant. Accurate mass measurement of a levitated nanomechanical resonator for precision force-sensing. *Nano Letters*, 19(10):6711–6715, 2019.

[36] J. Liu and K-D. Zhu. Highly sensitive mass detection using optically levitated microdisks. *IEEE Sensors Journal*, 19(17):7269–7274, 2019.

[37] S. K. Bera, A. Kumar, S. Sil, T. K. Saha, T. Saha, and A. Banerjee. Simultaneous measurement of mass and rotation of trapped absorbing particles in air. *Optics Letters*, 41(18):4356–4359, 2016.

[38] G. Carlse, A. Pouliot, T. Vacheresse, A. Carew, H. C. Beica, S. Winter, and A. Kumarakrishnan. Technique for magnetic moment reconstruction of laser-cooled atoms using direct imaging and prospects for measuring magnetic sublevel distributions. *Journal of the Optical Society of America B*, 37:1419, 2020.

[39] J. Blum, S. Bruns, D. Rademacher, A. Voss, B. Willenberg, and M. Krause. Measurement of the translational and rotational Brownian motion of individual particles in a rarefied gas. *Physical Review Letters*, 97(23):230601, 2006.

[40] A. Ashkin. Forces of a single-beam gradient laser trap on a dielectric sphere in the ray optics regime. *Biophysical Journal*, 61(2):569–582, 1992.

[41] D. R. Burnham. *Microscopic applications of holographic beam shaping and studies of optically trapped aerosols.* PhD thesis, University of St. Andrews, 2009.

[42] Y. Harada and T. Asakura. Radiation forces on a dielectric sphere in the Rayleigh scattering regime. *Optics Communications*, 124(5-6):529–541, 1996.

[43] J. P. Barton, D. R. Alexander, and S. A. Schaub. Internal and near-surface electromagnetic fields for a spherical particle irradiated by a focused laser beam. *Journal of Applied Physics*, 64(4):1632–1639, 1988.

[44] K. F. Ren, G. Greha, and G. Gouesbet. Radiation pressure forces exerted on a particle arbitrarily located in a gaussian beam by using the generalized lorenz-mie theory, and associated resonance effects. *Optics Communications*, 108(4-6):343–354, 1994.

[45] A. Rohrbach and E. H. K. Stelzer. Optical trapping of dielectric particles in arbitrary fields. *Journal of the Optical Society of America A*, 18(4):839–853, 2001.

[46] A. Rohrbach and E. H. K. Stelzer. Trapping forces, force constants, and potential depths for dielectric spheres in the presence of spherical aberrations. *Applied Optics*, 41(13):2494–2507, 2002.

[47] P. Langevin. Sur la théorie du mouvement Brownien. *Compt. Rendus*, 146: 530–533, 1908.

[48] R. Brown. XXVII. A brief account of microscopical observations made in the months of june, july and august 1827, on the particles contained in the pollen of plants; and on the general existence of active molecules in organic and inorganic bodies. *The Philosophical Magazine*, 4(21):161–173, 1828.

[49] A. Einstein. Investigations on the theory of the brownian movement. *Annalen Der Physik*, 17:549, 1905.

[50] G. E. Uhlenbeck and L. S. Ornstein. On the theory of the Brownian motion. *Physical Review*, 36(5):823, 1930.

[51] K. C. Neuman and S. M. Block. Optical trapping. *Review of Scientific Instruments*, 75(9):2787–2809, 2004.

[52] M. C. Wang and G. E. Uhlenbeck. On the theory of the Brownian motion ii. *Reviews of Modern Physics*, 17(2-3):323, 1945.

[53] S. Velasco. On the Brownian motion of a harmonically bound particle and the theory of a Wiener process. *European Journal of Physics*, 6(4):259, 1985.

[54] J. Bechhoefer and S. Wilson. Faster, cheaper, safer optical tweezers for the undergraduate laboratory. *American Journal of Physics*, 70(4):393–400, 2002.

[55] D. A. Weitz, D. J. Pine, P. N. Pusey, and R. J. A. Tough. Nondiffusive brownian motion studied by diffusing-wave spectroscopy. *Physical Review Letters*, 63(16):1747, 1989.

[56] J. X. Zhu, D. J. Durian, J. Müller, D. A. Weitz, and D. J. Pine. Scaling of transient hydrodynamic interactions in concentrated suspensions. *Physical Review Letters*, 68(16):2559, 1992.

[57] M. H. Kao, A. G. Yodh, and D. J. Pine. Observation of Brownian motion on the time scale of hydrodynamic interactions. *Physical Review Letters*, 70(2): 242, 1993.

[58] Y. Han, A. M. Alsayed, M. Nobili, J. Zhang, T. C. Lubensky, and A. G. Yodh. Brownian motion of an ellipsoid. *Science*, 314(5799):626–630, 2006.

[59] V. Vladimirsky and Y. A. Terletzky. Hydrodynamical theory of translational brownian motion. *Zhurnal Eksperimental'noy Teoreticheskoy Fiziki*, 15:258–263, 1945.

[60] E. J. Hinch. Applications of the langevin equation to fluid suspensions. *Journal of Fluid Mechanics*, 72(3):499–511, 1975.

[61] H. J. H. Clercx and P. P. J. M. Schram. Brownian particles in shear flow and harmonic potentials: A study of long-time tails. *Physical Review A*, 46(4): 1942–1950, 1992.

[62] B. J. Alder and T. E. Wainwright. Velocity autocorrelations for hard spheres. *Physical Review Letters*, 18(23):988, 1967.

[63] B. J. Alder and T. E. Wainwright. Decay of the velocity autocorrelation function. *Physical Review A*, 1(1):18, 1970.

[64] R. Zwanzig and M. Bixon. Hydrodynamic theory of the velocity correlation function. *Physical Review A*, 2(5):2005, 1970.

[65] B. R. Bzdek, L. Collard, J. E. Sprittles, A. J. Hudson, and J. P. Reid. Dynamic measurements and simulations of airborne picolitre-droplet coalescence in holographic optical tweezers. *Journal of Chemical Physics*, 145(5):054502, 2014.

[66] R. B. Bird, W. E. Stewart, and E. N. Lightfoot. *Transport Phenomena*. John Wiley and Sons Inc., 2nd edition, 2007.

[67] L. Gilchrist. An absolute determination of the viscosity of air. *Physical Review*, 1(2):124, 1913.

[68] H. C. Beica, A. Pouliot, A. Carew, A. Vorozcovs, N. Afkhami-Jeddi, G. Carlse, P Dowling, B. Barron, and A. Kumarakrishnan. Characterization and applications of auto-locked vacuum-sealed diode lasers for precision metrology. *Review of Scientific Instruments*, 90(8):085113, 2019.

[69] A. Pouliot, H. C. Beica, A. Carew, A. Vorozcovs, G. Carlse, and A. Kumarakrishnan. Auto-locking waveguide amplifier system for lidar and magnetometric applications. In *High-Power Diode Laser Technology XVI*, volume 10514, page 105140S. International Society for Optics and Photonics, 2018.

[70] T. Polster, S. Leopold, and M. Hoffmann. Airborne particle generation for optical tweezers by thermo-mechanical membrane actuators. In *Smart Sensors, Actuators, and MEMS V*, volume 8066, page 80661F. International Society for Optics and Photonics, 2011.

[71] M. Esseling, P. Rose, C. Alpmann, and C. Denz. Photophoretic trampoline—interaction of single airborne absorbing droplets with light. *Applied Physics Letters*, 101(13):131115, 2012.

[72] Vision Research: Phantom Ultra High-Speed UHS-12 Camera Line Data Sheet. www.phantomhighspeed.com/products/cameras/ultrahighspeed/v2012. Accessed: 2020-04-05.

[73] C. D. Wallace, T. P Dinneen, K-Y. N. Tan, A. Kumarakrishnan, P L. Gould, and J. Jananainen. Measurements of temperature and spring constant in a magneto-optical trap. *Journal of the Optical Society of America B*, 11(5): 703–711, 1994.

[74] R. Huang. *Brownian motion at fast time scales and thermal noise imaging.* PhD thesis, University of Texas at Austin, 2008.

[75] T. Li. *Fundamental tests of physics with optically trapped microspheres.* PhD thesis, University of Texas at Austin, 2008.

[76] N. Chenouard, I. Smal, F. De Chaumont, M. Maška, I. F. Sbalzarini, Y. Gong, J. Cardinale, C. Carthel, S. Coraluppi, M. Winter, et al. Objective comparison of particle tracking methods. *Nature Methods*, 11(3):281, 2014.

[77] A. J. Berglund, M. D. McMahon, J. J. McClelland, and J. A. Liddle. Fast, bias free algorithm for tracking single particles with variable size and shape. *Optics Express*, 16(18):14064–14075, 2008.

[78] R. M. Power, D. R. Burnham, and J. P. Reid. Toward optical-tweezers-based force microscopy for airborne microparticles. *Applied Optics*, 53(36):8522–8534, 2014.

[79] J. Lin, A. G. Hart, and Y-Q. Li. Optical pulling of airborne absorbing particles and smut spores over a meter-scale distance with negative photophoretic force. *Applied Physics Letters*, 106(17):171906, 2015.

[80] J. Lin and Y-Q. Li. Optical trapping and rotation of airborne absorbing particles with a single focused laser beam. *Applied Physics Letters*, 104(10):101909, 2014.

[81] X. Chen, L. Ren, Y. Qiu, and Liu H. New method for determining the depth of field of microscope systems. *Applied Optics*, 50(28):5524–5533, 2011.

[82] H. Flyvbjerg and H. G. Petersen. Error estimates on averages of correlated data. *Journal of Chemical Physics*, 91(1):461–466, 1998.

[83] G. Spirou, I. Yavin, M. Weel, A. Vorozcovs, A. Kumarakrishnan, P. R. Battle, and R. C. Swanson. A high-speed-modulated retro-reflector for lasers using an acousto-optic modulator. *Canadian Journal of Physics*, 81(4):625–638, 2003.

[84] I. D. van der Werf, G. Germinario, F. Palmisano, and L. Sabbatini. Characterisation of permanent markers by pyrolysis gas chromatography–mass spectrometry. *Analytical and Bioanalytical Chemistry*, 399(10):3483–3490, 2011.

[85] E. J. G. Peterman, F. Gittes, and C. F. Schmidt. Laser-induced heating in optical traps. *Biophysical Journal*, 84(2):1308–1316, 2003.

[86] D. McGloin, D. R. Burnham, M. D. Summers, D. Rudd, N. Dewar, and S. Anand. Optical manipulation of airborne particles: techniques and applications. *Faraday Discussions*, 137:335–350, 2008.

[87] A. Ashkin and J. M. Dziedzic. Optical trapping and manipulation of viruses and bacteria. *Science*, 235(4795):1517–1520, 1987.

[88] Y. Pang, H. Song, J. H. Kim, X. Hou, and W. Cheng. Optical trapping of individual human immunodeficiency viruses in culture fluid reveals heterogeneity with single-molecule resolution. *Nature Nanotechnology*, 9(8):624, 2014.

[89] Z. Zhang, T. E. P. Kimkes, and M. Heinemann. Manipulating rod-shaped bacteria with optical tweezers. *Scientific Reports*, 9(1):1–9, 2019.